OPEN ACCESS



BASS. LII. The Prevalence of Double-peaked Broad Lines at Low Accretion Rates among Hard X-Ray Selected Active Galactic Nuclei

Charlotte Ward 1 , Michael J. Koss 2,3 , Michael Eracleous 4 , Benny Trakhtenbrot 5 , Franz E. Bauer 6 , Turgay Caglar 7,8 , Fiona Harrison 9 , Arghajit Jana 10 , Darshan Kakkad 11 , Macon Magno 7,12 , Ignacio del Moral-Castro 13 , Richard Mushotzky 14,15 , Kyuseok Oh 6 , Alessandro Peca 2,17 , Meredith C. Powell 18 , Claudio Ricci 10,19 , Alejandra Rojas 20 , Krista Lynne Smith 10 , Daniel Stern 2 , Ezequiel Treister 6 , and C. Megan Urry 17,23

1 Department of Astronomy & Astrophysics, 525 Davey Lab, 251 Pollock Road, The Pennsylvania State University, University Park, PA 16802, USA; cvw5890@psu.edu ² Eureka Scientific, 2452 Delmer Street, Suite 100, Oakland, CA 94602-3017, USA ³ Space Science Institute, 4750 Walnut Street, Suite 205, Boulder, CO 80301, USA ⁴ Department of Astronomy & Astrophysics and Institute for Gravitation and the Cosmos, 525 Davey Lab, 251 Pollock Road, The Pennsylvania State University, University Park, PA 16802, USA ⁵ School of Physics and Astronomy, Tel Aviv University, Tel Aviv 69978, Israel 6 Instituto de Alta Investigación, Universidad de Tarapacá, Casilla 7D, Arica, Chile George P. and Cynthia Woods Mitchell Institute for Fundamental Physics and Astronomy, Texas A&M University, College Station, TX 77845, USA Leiden Observatory, PO Box 9513, 2300 RA Leiden, The Netherlands ⁹ Cahill Center for Astronomy and Astrophysics, California Institute of Technology, Pasadena, CA 91125, USA Instituto de Estudios Astrofísicos, Facultad de Ingeniería y Ciencias, Universidad Diego Portales, Av. Ejército Libertador 441, Santiago, Chile

11 Centre for Astrophysics Research, University of Hertfordshire, College Lane, Hatfield, AL10 9AB, UK

12 CSIRO Space and Astronomy, ATNF, PO Box 1130, Bentley WA 6102, Australia 13 Instituto de Astrofísica, Facultad de Física, Pontificia du Universidad Católica de Chile, Av. Vicuia Mackenna 4860, Santiago, Chile Department of Astronomy, University of Maryland, College Park, MD 20742, USA ¹⁵ Joint Space-Science Institute, University of Maryland, College Park, MD 20742, USA ¹⁶ Korea Astronomy and Space Science Institute, Daedeokdae-ro 776, Yuseong-gu, Daejeon 34055, Republic of Korea Department of Physics, Yale University, P.O. Box 208120, New Haven, CT 06520, USA 18 Leibniz-Institut für Astrophysik Potsdam (AIP), An der Sternwarte 16, 14482 Potsdam, Germany ¹⁹ Kavli Institute for Astronomy and Astrophysics, Peking University, Beijing 100871, People's Republic of China ²⁰ Departamento de Física, Universidad Técnica Federico Santa María, Vicuña Mackenna 3939, San Joaquín, Santiago de Chile, Chile ²¹ George P. and Cynthia Woods Mitchell Institute for Fundamental Physics and Astronomy, Texas A&M University, College Station, TX 77843-4242, USA ²² Jet Propulsion Laboratory, California Institute of Technology, 4800 Oak Grove Drive, MS 169-224, Pasadena, CA 91109, USA Yale Center for Astronomy & Astrophysics and Department of Physics, Yale University, P.O. Box 208120, New Haven, CT 06520-8120, USA Received 2025 June 10; revised 2025 July 25; accepted 2025 July 28; published 2025 September 19

Abstract

A fraction of active galactic nuclei (AGN) have double-peaked $H\alpha$, $H\beta$, and Mg II broad lines attributed to emission from rotating gas in the accretion disk. Using optical spectroscopy of a flux-limited sample of AGN selected via ultrahard X-rays from the BAT AGN Spectroscopic Survey (BASS), we systematically identify 71 double-peaked emitters (DPEs) among 343 broad-line AGN with redshifts 0.004 < z < 0.297 and X-ray luminosities of $40 < \log L_{2-10 \text{KeV}} (\text{erg s}^{-1}) < 45.7$, and provide their best-fit accretion disk parameters. We find that $\sim 21\%$ of X-ray-selected broad-line AGN are DPEs, consistent with rates previously reported for z < 0.2 broad-line AGN selected for strong optical variability in the Zwicky Transient Facility. 11 of 71 DPEs (15%) exhibited a singlepeaked Gaussian component to the broad line profile in addition to the double-peaked disk profile. In this sample, DPEs have intrinsically higher masses by ~ 0.4 dex and lower Eddington ratios by ~ 0.3 dex than other broad-line AGN, and have a preference for elliptical host galaxies, higher X-ray luminosities, and higher [O I] $\lambda 6302$ to narrow $H\alpha$ flux ratios than other broad-line AGN. We find that DPEs are not segregated from non-DPE broad-line AGN in the $L_{\rm bol}$ versus $M_{\rm BH}$ relation or their X-ray to radio luminosity ratios, and do not show a preference for intermediate Seyfert types over Seyfert 1s. We do not find differences in a wide range of multiwavelength properties when comparing DPEs to non-DPE broad-line AGN, including optical and mid-IR variability levels, Wide-field Infrared Survey Explorer colors, α_{ox} , the column density of neutral obscuring material N_{H} , and the rate of changing-look events. We discuss the two populations in the context of multicomponent disk-wind models of the AGN broad-line region and consider how unrecognized contributions of disk emission to the broad lines may introduce biases in "virial" supermassive black hole mass estimates, with consequences for the inferred $M_{\rm BH}$ - M_* relation.

Unified Astronomy Thesaurus concepts: AGN host galaxies (2017); Active galaxies (17); Supermassive black holes (1663)

Materials only available in the online version of record: figure set, machine-readable tables

1. Introduction

Understanding how today's supermassive black holes (SMBHs) first formed, grew over time, and coevolved with their host galaxies is key to many open questions in modern astrophysics (e.g., J. E. Greene et al. 2020). Yet, we still do not

understand the geometry of accretion flows and "broad-line region" (BLR) gas within thousands of gravitational radii of active galactic nuclei (AGN). It is known from reverberation mapping campaigns that the motion of the BLR is not predominantly radial (see B. M. Peterson 1993, for a review) and that the BLR is virialized (B. M. Peterson & A. Wandel 2000; W. Kollatschny 2003). A range of models for the BLR have invoked the outer part of the accretion disk as a key component, including models of clouds flowing away from the disk along magnetic field lines (R. T. Emmering et al. 1992), radiatively accelerated winds (N. Murray et al. 1995), and combined contributions of an accretion disk and an additional gaseous region (L. Č. Popović et al. 2004). Yet, several mysteries, including how super-Eddington accretion might grow the overmassive SMBHs discovered by the James Webb Space Telescope at $z \approx 10$ (A. D. Goulding et al. 2023), and how AGN broad Balmer emission lines appear and disappear on human timescales in "changing-look" events (C. Ricci & B. Trakhtenbrot 2023), motivate us to understand how BLR structure depends on accretion rate, and how viewing angle affects the observable properties of broad-line AGN populations across redshift.

A key subpopulation of AGN that can provide constraints for various BLR models is the double-peaked emitters (DPEs). DPEs are typically observed to have H α , H β , and Mg II λ 2798 broad lines with two shoulders that are blueshifted and redshifted from the rest velocity by a few hundred to a few thousand kilometers per second due to the Keplerian motion of gas within a disk spanning a few hundred to a few thousand gravitational radii (M. Eracleous & J. P. Halpern 1994; K. Chen & J. P. Halpern 1989; M. Eracleous et al. 1997, 2009; I. V. Strateva et al. 2003). Models applied to fit the broad-line profile shapes of DPEs depend on factors such as disk inclination angle, turbulent broadening, the disk emissivity as a function of radius, and radiative transfer through the base of a wind (K. Chen & J. P. Halpern 1989; N. Murray & J. Chiang 1996; I. V. Strateva et al. 2003; H. M. L. G. Flohic et al. 2012; L. S. Chajet & P. B. Hall 2013; K. Nguyen et al. 2018). While the Balmer series and the Mg II $\lambda 2798$ lines in DPEs usually have double-peaked profiles that can be described by the same disk model for a given source, UV resonance lines, such as Ly α and C IV, which have much higher optical depth, have single-peaked profiles due to their higher optical depth and, in the case of Ly α , collisional de-excitation in the dense emission region (M. Eracleous et al. 2009, and references therein). While the binary SMBH interpretation is sometimes invoked for double-peaked profiles, this model cannot explain line profile variability observed in the majority of DPEs (A. Doan et al. 2020, and references therein) and has been ruled out for some DPE samples by the observation of single-peaked Ly α broad lines (J. C. Runnoe et al. 2025).

DPEs are most commonly identified in low-luminosity, low-accretion rate AGN (M. Eracleous & J. P. Halpern 1994, 2003; L. C. Ho et al. 2000; L. C. Ho 2008). A two-component disk-wind structure may account for a transition to a "disk-dominated" state at low luminosities (M. Elitzur & L. C. Ho 2009; M. Elitzur et al. 2014). In this model, the BLR consists of an outflow of gas embedded in a hydromagnetic disk wind. When the gas is released from the disk, it expands and reduces in column density, resulting in a toroidal geometry for both the BLR and the dusty torus beyond the dust sublimation radius (R. T. Emmering et al. 1992; H. Netzer & A. Laor 1993;

M. Elitzur & I. Shlosman 2006; B. Czerny et al. 2015, 2016). The outflowing, low column density gas produces broad Gaussian lines, while high-density gas close to the disk surface rotating at Keplerian velocities produces the double-peaked emission. As the accretion rate decreases, the BLR structure loses its components at the highest elevations above the disk, and the double-peaked emission from the disk could increasingly dominate over Gaussian broad-line emission. This model may also explain the DPE preference for intermediate-type Seyferts over Seyfert 1s (Sy1s; M. Elitzur & L. C. Ho 2009; M. Elitzur et al. 2014). In order to test this model, we need to disentangle viewing angle effects, accretion rate effects, and AGN population selection biases, motivating the systematic classification of DPE subsamples among AGN selected by different means.

Distinguishing between intrinsic differences in BLR geometry and viewing angle effects is challenging. T. Storchi-Bergmann et al. (2017) consider that if double-peaked profiles are ubiquitous in broad-line AGN, but are usually only observed when the inclination angle is $\gtrsim 20^{\circ}$ so that the separate peaks of the accretion disk are observable, but $\lesssim 37^{\circ}$ so that the accretion disk emission is not blocked by the obscuring torus, this would result in an observed ~60% fraction of broad-line AGN with double peaks, which is much higher than the observed DPE rate. It is clear that outflowing gas must dominate broad-line emission in most AGN, even if an additional disk emission line is present. It is known that some AGN have both a Gaussian BLR component and a disk component. This has been identified in SDSS J125809.31+351943.0, for example, which varied in Eddington ratio from 0.4% to 2.4%, and exhibited a primarily double-peaked H β profile during dim periods and a singlepeaked profile during bright periods (S. Nagoshi et al. 2024). Analysis of the "rms" spectra derived from multi-epoch observations of some AGN has also often shown a doublepeaked H β profile, implying the presence of variable, disk-like gas that may not be clear from a single-epoch spectrum that appears single peaked (K. D. Denney et al. 2010; J. S. Schimoia et al. 2017; T. Storchi-Bergmann et al. 2017).

DPEs may be an important source of population-level bias in virial black hole (BH) mass ($M_{\rm BH}$) measurements (X. Wu & F. K. Liu 2004; K. T. Lewis & M. Eracleous 2006; W. Bian et al. 2007; Y. Fu et al. 2023). A key method to measure $M_{\rm BH}$ for unobscured AGN is the "virial" method, whereby the width of the H α , H β , or other broad emission lines is used as a proxy for the virial velocity of the BLR gas (e.g., J. E. Greene & L. C. Ho 2005, and references therein). By adopting the empirical relation between the BLR size and the continuum luminosity and the emission-line width of the broad component, BH masses can be calculated (S. Kaspi et al. 2000; M. C. Bentz et al. 2009). While this method has been effective in determining the BH mass function and probing the relationship between $M_{\rm BH}$ and the stellar velocity dispersion of the host galaxy (the $M_{\rm BH}$ - σ_* relation) for populations of unobscured AGN over a range of redshifts (e.g., Y. Shen et al. 2008, 2019; H. Übler et al. 2023; M. Mezcua et al. 2024), it is sensitive to various biases that may affect $M_{\rm BH}$ measurements by $\gtrsim 0.4$ dex (Y. Shen 2013; B. M. Peterson 2014; T. Caglar et al. 2020), including the virial factor f, which introduces uncertainties of 0.12 dex (J.-H. Woo et al. 2015), intrinsic scatter of the BLR radius-luminosity relation, which introduces scatter of order 0.1 dex (M. C. Bentz et al. 2009), and variability in both the AGN continuum luminosity and the broad-line width (D. Park et al. 2012). DPEs have been

identified in various studies where they have also inhibited accurate virial mass measurements for those objects, including in samples of hard X-ray-selected AGN in the local Universe, where 29 out of $\sim\!600$ AGN were identified as DPE candidates (J. E. Mejía-Restrepo et al. 2022), as well as in James Webb Space Telescope studies of z>6 AGN, where one in a sample of 12 was identified as a DPE (M. Onoue et al. 2024). It is therefore important to understand the fraction of broad-line AGN that are DPEs, methods to identify them, and the extent to which they may introduce biases or scatter in the $M_{\rm BH}\!-\!\sigma_*$ relation.

Estimates of DPE fractions among the wider broad-line AGN population range from \sim 3% to 30% (M. Eracleous & J. P. Halpern 1994; L. C. Ho et al. 1997; I. V. Strateva et al. 2003; C. Ward et al. 2024), depending on how the AGN sample is selected and the criteria used to distinguish between DPEs and non-DPE broad-line AGN. Notably, the DPE rate was found to be 19% among z < 0.4 AGN with strong (>1.5 mag) optical variability in the Zwicky Transient Facility (ZTF; E. C. Bellm et al. 2019; M. J. Graham et al. 2019; R. Dekany et al. 2020) photometry (C. Ward et al. 2024). Comparison of ZTF light curve power spectra from DPEs and other variable AGN did not find significant differences in variability amplitude or power law index (C. Ward et al. 2022), despite previous work from X.-G. Zhang & L.-L. Feng (2017) finding that DPE light curves from the Catalina Sky Survey (A. J. Drake et al. 2009) had damped random walk characteristic timescales 2.7 times longer than a control sample's Sloan Digital Sky Survey (SDSS) Stripe 82 (D. M. Bramich et al. 2008) light curves. DPEs show some clearer differences to other broad-line AGN when considering their host galaxies and X-ray/radio properties: DPEs are preferentially associated with radio-loud elliptical hosts with large bulge and BH masses (M. Eracleous & J. P. Halpern 1994, 2003), and DPE radio and soft X-ray luminosities are \sim 1.5 times higher than the control samples (I. V. Strateva et al. 2003).

The BAT AGN Spectroscopic Survey²⁴ (BASS) provides a comprehensive data set of optical and NIR spectroscopy for a sample of ~1000 AGN selected via ultra-hard X-rays (14-195 keV) in the Swift/Burst Alert Telescope (BAT) mission (M. Koss et al. 2017; M. J. Koss et al. 2022b). This well-studied sample provides an opportunity to estimate DPE rates in a hard X-ray flux-limited AGN population that is not biased by viewing angle effects, and to study their multiwavelength properties compared to other broad-line AGN. This paper is structured as follows. Section 2 outlines our modeling of optical spectra of the BASS AGN sample to distinguish between DPEs and other broad-line AGN and characterize their disk properties. In Section 3, we discuss the construction of optical ZTF light curves and mid-IR Wide-field Infrared Survey Explorer (WISE; E. L. Wright et al. 2010) light curves and variability metrics. In Section 4, we compare various X-ray, IR, and radio characteristics of the DPEs and other broad-line AGN in the BASS sample. In Section 5, we discuss the stellar masses of the DPEs and other broad-line AGN, and discuss possible biases in the virial masses measured for DPE candidates. Section 6 discusses the host galaxy properties of the two samples. Section 7 discusses the implications of our results for the disk-wind model and possible future work. We summarize our conclusions in Section 8. Throughout this paper, we adopt the WMAP7 cosmology with $H_0 = 70.4$ and $\Omega_m = 0.272$ (E. Komatsu et al. 2011).

2. Disk Profile Fitting for BASS Broad-line AGN

With the goal of identifying DPEs among BASS broad-line AGN using the H α line, we began with a sample of 742 hard X-ray-selected AGN with rest-frame optical line measurements reported in the BASS DR2 Spectroscopic Line Measurements Catalog (K. Oh et al. 2022). We excluded 196 Type 2 AGNs from the sample. Following the methods described in C. Ward et al. (2024), we used penalized pixel fitting (pPXF; M. Cappellari & E. Emsellem 2003; M. Cappellari 2017) to model and subtract the stellar continuum and absorption lines. After removing 179 objects that did not have H α line coverage in the BASS spectra or had data reduction artifacts preventing the production of a reasonable continuum model, we obtained a sample of 367 AGN. We note here that the H β broad line can also be used to constrain disk parameters, but as the H α profiles had a higher signal-to-noise ratio (S/N) and we wished to compare to previous work from H α fitting of variability-selected DPEs from ZTF (C. Ward et al. 2024), we decided to focus only on objects with available H α to ensure uniformity in the fitting procedure across samples. We further excluded 24 objects with low S/N broad lines that would prevent a meaningful disk model fit. We did not apply a particular S/N cut, but instead decided on whether there was a sufficient S/N based on the posteriors obtained from the disk model fitting described in the next paragraph—if the broad-line parameters were entirely unconstrained, we removed them from the sample. This process provided a sample of 343 broad-line AGN for H α fitting. The final sample of 343 AGN is representative of BASS unobscured AGN within a redshift range of 0.004–0.3. Using the galaxy morphology classifications reported in M. Parra Tello et al. (2025), 116 of the host galaxies were reported as having "smooth" (elliptical) morphologies, 44 are mergers, 97 are "disk" galaxies, 16 were edge-on galaxies, 29 were "pointlike," and 38 fell into the "uncertain/other" category.

After continuum subtraction, we modeled the broad $H\alpha$ of each AGN with the circular accretion disk model from K. Chen & J. P. Halpern (1989). We followed the procedure established for disk model fitting of the ZTF AGN sample in C. Ward et al. (2024), but we reiterate the procedure here for completeness. The disk model has the following free parameters: the inclination angle i (deg) where 0° is face-on and 90° is edge-on, a local turbulent broadening parameter σ (km s^{-1}) , the emissivity power law index q where the emissivity varies with radius as $\epsilon \propto r^{-q}$, and the inner and outer dimensionless inner and outer radii of the disk ξ_1 and ξ_2 expressed relative to the gravitational radius, $GM_{\rm BH}/c^2$. We enabled a single spiral arm with free parameters amplitude A_s (expressed as a contrast ratio relative to the rest of the disk), orientation angle ϕ_0 (deg), width w (deg), and pitch angle ψ (deg). This was required to describe the flux ratio of the red and blue shoulders being >1 in a fraction of spectra, which has been commonly observed in other disk emitters (e.g., T. Storchi-Bergmann et al. 2003). We applied the following bounds on some parameters via a uniform prior: $\xi_1 > 50$, w < 80, $0 < \psi < 60$, and $A_s < 1$, based on typical parameters

²⁴ https://bass-survey.com

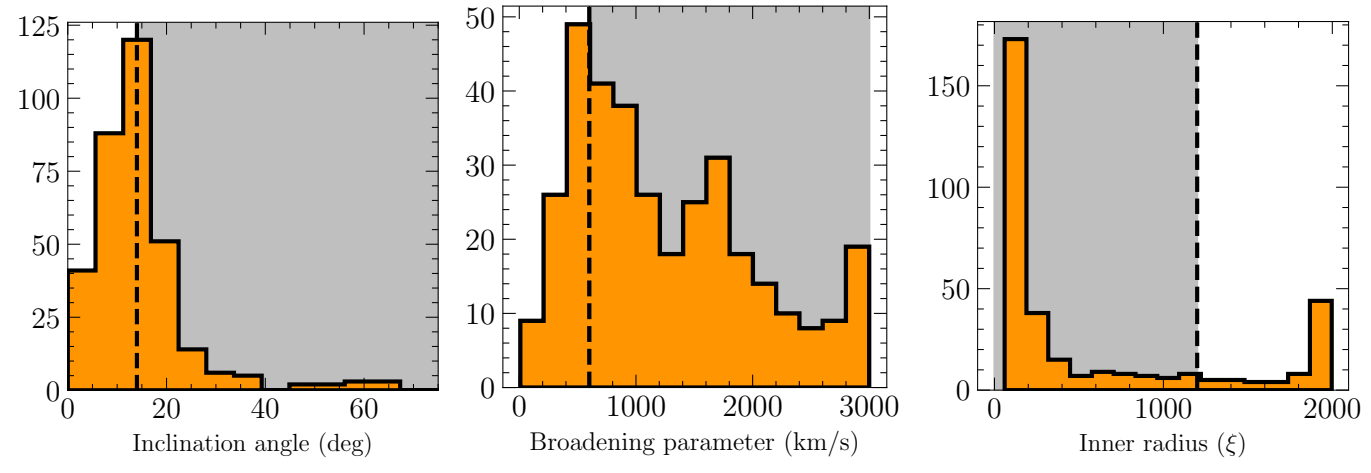


Figure 1. Histograms showing the distributions of the three disk parameters used to separate DPEs from AGN without double-peaked broad lines. DPEs were classified as those with inclination angle >14°, turbulent broadening >600 km s⁻¹, and inner radius <1200 gravitational radii, corresponding to the gray shaded regions to the right of the vertical dashed lines in the left and center plots, and to the left of the vertical dashed line in the right plot.

found for DPEs with detailed spiral arm modeling of multiepoch spectra (e.g., J. S. Schimoia et al. 2012, 2017).

The disk model was fitted simultaneously with a model for the forbidden narrow emission lines overlapping the broad H α line. The [S II] $\lambda\lambda6718$, 6733, [N II] $\lambda\lambda6550$, 6585, and [O I] $\lambda\lambda$ 6302, 6366 doublet flux ratios (where we report vacuum wavelengths) were fixed to theoretical values of 0.77, 0.34, and 3.0, respectively (D. E. Osterbrock & G. J. Ferland 2006). We note that the [SII] ratio can vary between 0.4 and 1.4, but we choose to fix it to reduce the number of free parameters, as it is usually close to the wing of the H α line, where it does not significantly affect the disk parameters. Each individual narrow line was described by two Gaussian components of the same central wavelength with three free parameters that were common for all narrow lines: the velocity dispersion of the first Gaussian component σ_1 , the velocity dispersion of the second Gaussian component σ_2 , and the flux ratio of the two components f_1/f_2 . The amplitudes of the spectral lines are linear parameters, and so for computational expediency, we used a profile likelihood technique in which, for a given set of narrow-line, broad-line, and disk model parameters, we determined the amplitudes via least-squares optimization.

We first found a reasonable initial fit using the nonlinear least-squares optimization implemented in Python using the SciPy package. We then explored the posteriors using emcee (D. Foreman-Mackey et al. 2013) with 60 walkers initialized at the best-fit values from the least-squares fit, distributed according to the 1σ error found from the leastsquares covariance matrix. For each spectrum, the emcee fitting was run for 2400 iterations after a burn-in time of 1800 iterations. The long burn-in phase was required for the chains to converge, given the large number of parameters. If no combination of parameters could account for the difference between the red and blue shoulder peak fluxes, we repeated the fitting prescription with greater freedom assigned to the spiral arm amplitude, increasing the amplitude from 1 to 10. While the spiral arm is well motivated for a subset of DPEs and has been shown to be a physically motivated way to account for profile variability in a subset of DPEs (J. S. Schimoia et al. 2017), the spiral arm can introduce significant flexibility in the shape of the disk profile, so we did not enable it to have a large amplitude by default and only applied the additional freedom as necessary. If increasing the maximum allowed spiral amplitude still did not enable a reasonable fit to the data, and there was evidence for an additional single-peaked component at the rest wavelength, we repeated the fitting procedure while also allowing for an additional single-peaked broad-line component modeled as a Gaussian of adjustable width and flux centered on the ${\rm H}\alpha$ rest velocity.

Following the guidelines established in C. Ward et al. (2024) to separate double-peaked broad lines from typical broad lines with no evidence for shoulders or asymmetries, we classified objects as DPEs if they had an inclination angle $i > 14^{\circ}$, turbulent broadening $\sigma > 600 \,\mathrm{km \, s^{-1}}$, and inner radius ξ_1 < 1200. This procedure was established in C. Ward et al. (2024) as disk models that meet these requirements have broad-line profiles where two separate shoulders are not blended. The distribution of these three parameters for the BASS sample and the DPE cutoffs is shown in Figure 1. This procedure led to 102 AGN classified as DPEs and the remaining 241 classified as "non-DPE" broad-line AGN, i.e., profiles with no evidence for two shoulders in the broad-line profile due to disk emission. We visually inspected the disk profile fits to the spectra, and reassigned 46 DPE candidates as likely AGN without disk profiles but instead with outflows causing asymmetries that produced disk model parameters consistent with a DPE. We reassigned 15 objects classified as non-DPEs to the DPE class, based on the presence of a dip in shoulders or a clear shoulder on the red or blue side of the profile. This resulted in the sample being split into 71 (21%) DPEs and 272 (79%) non-DPEs. We summarize the properties of the two samples in Figure 2, where we show the redshifts, the bolometric luminosities derived from intrinsic luminosity in the 14-150 keV14-150 keV range (C. Ricci et al. 2017; M. J. Koss et al. 2022a), and the host galaxy morphology classifications from M. Parra Tello et al. (2025). The BH masses of the two samples are discussed in Section 5. We note that 21 DPEs required a high amplitude spiral arm, and 11 required an additional broad Gaussian component. Examples of BASS AGN classified as DPEs and their broad-line models are shown in Figure 3. In addition, we show the models of 11 DPEs that required an additional Gaussian broad line in Figure 4. We emphasize that this criterion may miss the identification of low inclination angle DPEs, where the shoulders are sufficiently close together such that the profile appears single peaked. We may also miss DPEs where the

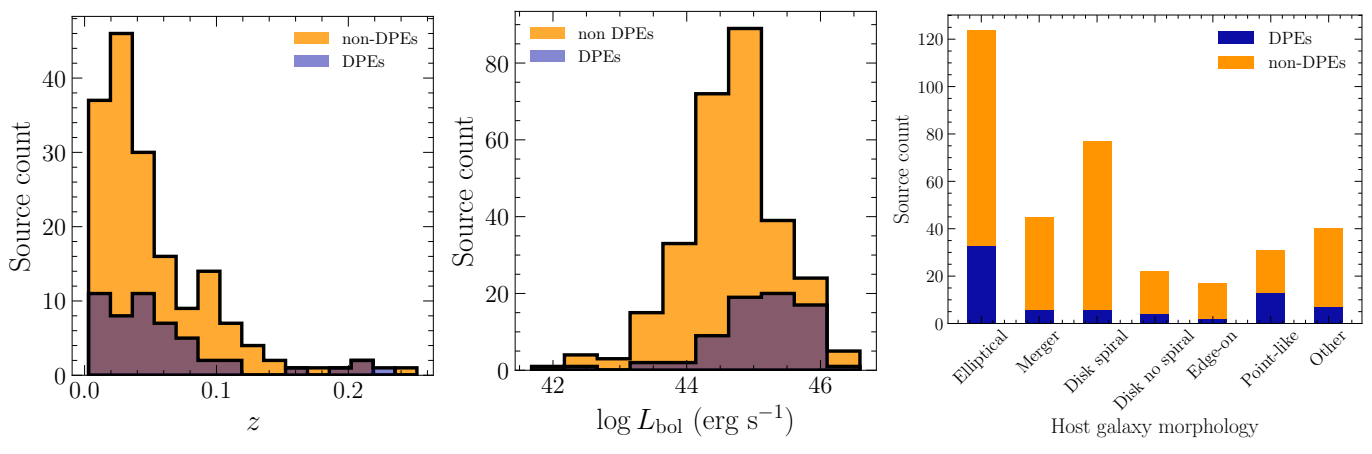


Figure 2. Properties of the parent sample after splitting into DPEs and non-DPE AGN: redshift (left), bolometric luminosity derived from the 14–150 keV intrinsic luminosities (center), and host galaxy types according to the classifications of M. Parra Tello et al. (2025) (right).

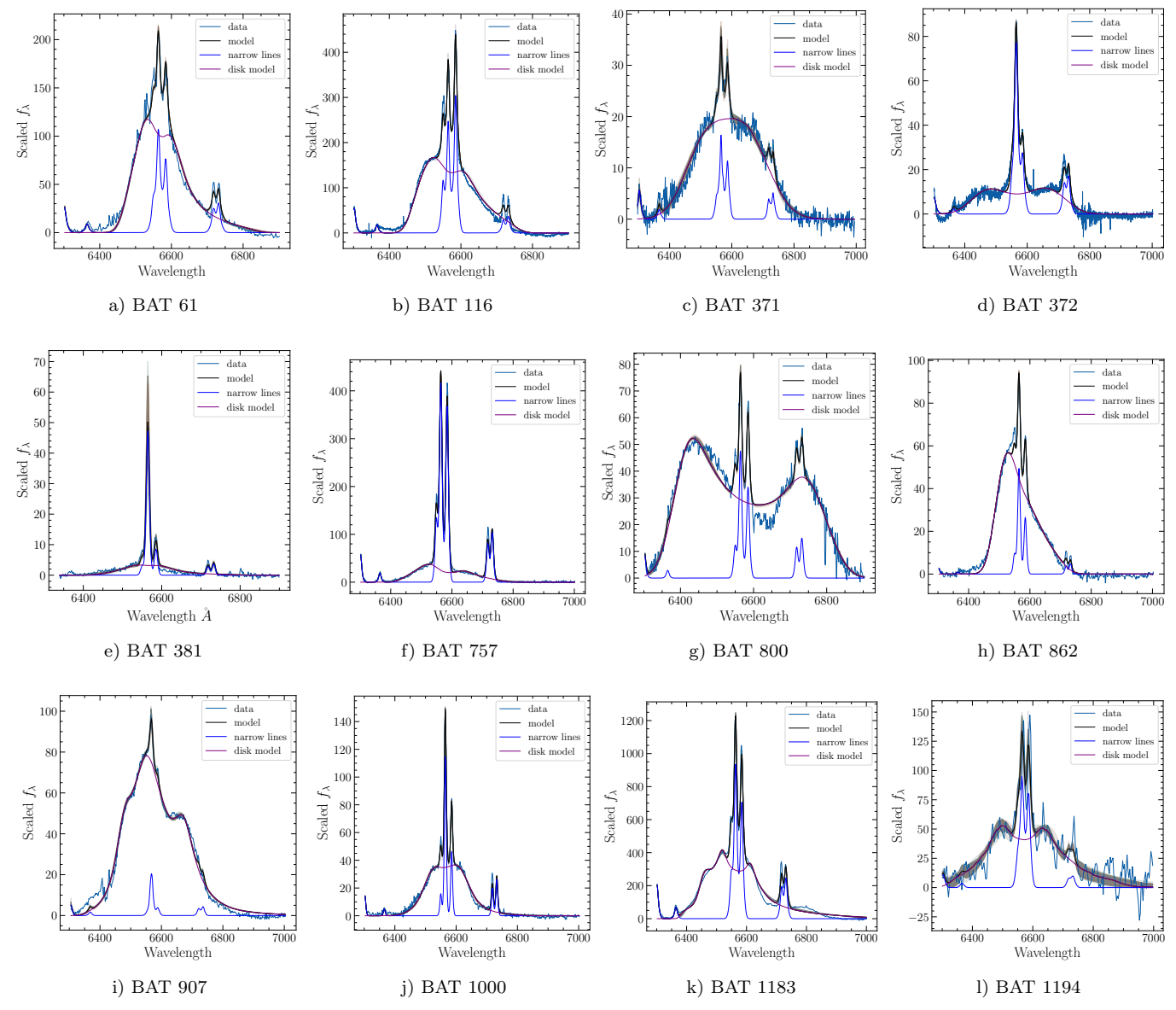


Figure 3. Examples of different disk profile morphologies for 12 DPEs identified in the parent sample for DPEs where an additional Gaussian broad-line component was not required to produce a good fit. We show the data from the continuum-subtracted spectrum reported in blue, the best-fit narrow-line component in dark blue, the disk model component in purple, and the summed model in black. The gray band around the total Markov Chain Monte Carlo (MCMC) model shows the distribution of total model fluxes when taking 100 random samples of the MCMC walkers after convergence. It therefore reflects the range of possible models within the reported parameter uncertainties. Disk profile fits for 61 DPEs are available in the online journal.

(The complete figure set (61 images) is available in the online article.)

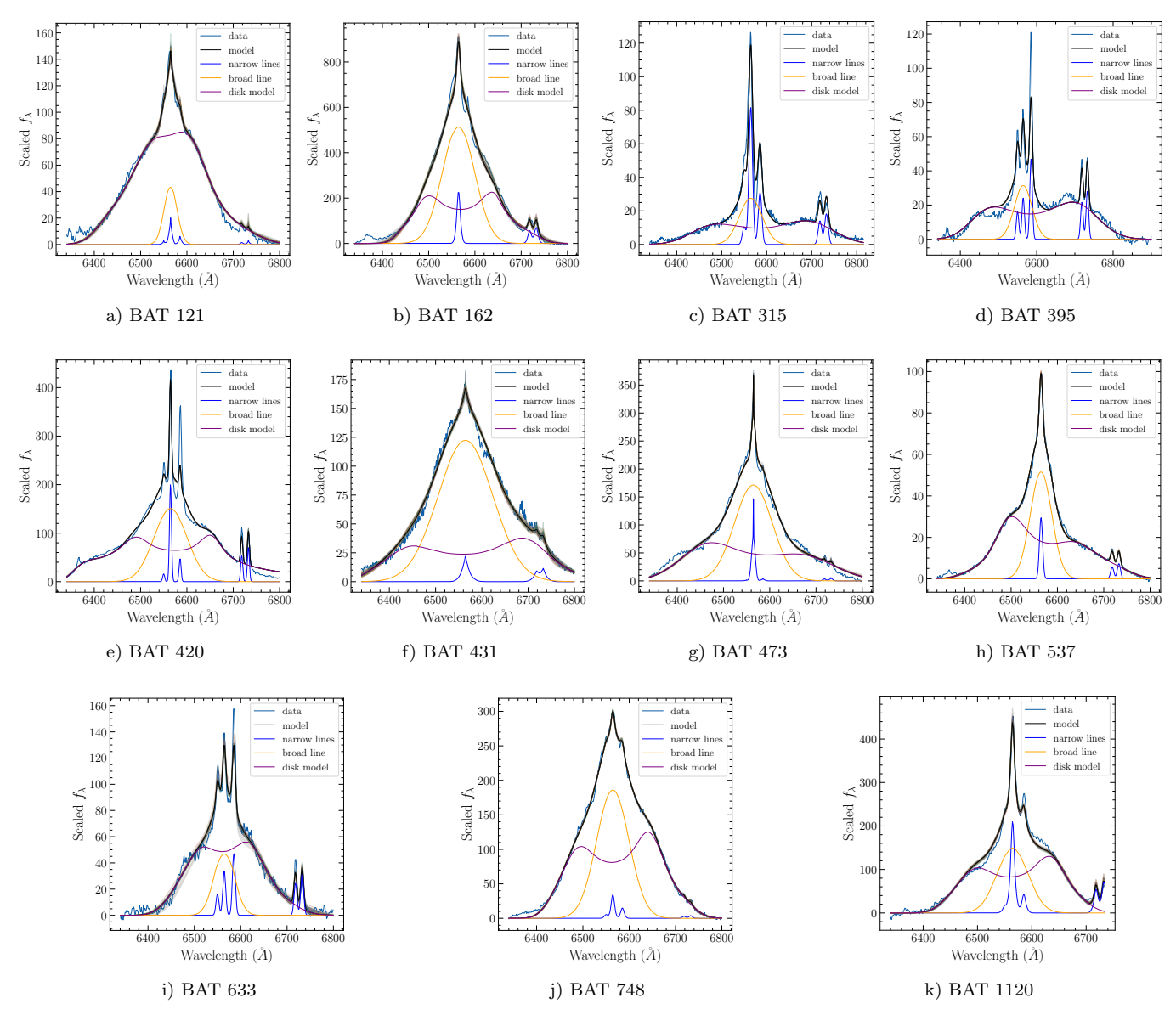


Figure 4. Disk profile morphologies for the 11 DPEs identified in the parent sample, where an additional Gaussian broad-line component was required to produce a good fit. We show the data from the continuum-subtracted spectrum reported in blue, the best-fit narrow-line component in dark blue, the disk model component in purple, the additional Gaussian broad line in orange, and the summed model in black. The gray band around the total model shows the distribution of total model fluxes when taking 100 random samples of the MCMC walkers after convergence. It therefore reflects the range of possible models within the reported parameter uncertainties

combination of the radii and the level of turbulent broadening hides the presence of two shoulders. The sample of non-DPE broad-line AGN may therefore have some contamination from unidentifiable DPEs, and the 21% DPE fraction should be considered a lower limit.

We note that in some cases (e.g., BAT 116, BAT 395) complex substructures in the broad-line profile are not fully modeled by the simple disk model: further free parameters for disk substructures like spiral arms or disk winds would allow the models to better match the data, but we do not add these additional parameters to avoid overfitting. In the case of BAT 800, the dip on the red side of the ${\rm H}\alpha+[{\rm N\,II}]$ complex is caused by imperfect correction of the telluric "A band." As has been demonstrated in previous fits of Arp 102B and others, it is the width of the profile and the separation of the shoulders that are most constraining on inclinations and disk radii (K. Chen & J. P. Halpern 1989; I. V. Strateva et al. 2003;

M. Eracleous et al. 2009), so we report the best-fit disk parameters for objects where these features of the profile shape were well described by the disk model. For one object, BAT 744, no model was found that adequately described the blueshifted broad line, so we do not report its disk parameters. The DPE sample is summarized in Table 1, and the non-DPE broad-line AGN sample (consisting of the remaining objects) is summarized in Table 4 in the Appendix. The best-fit disk parameters, details about their BASS spectrum, and an indication of whether an additional broad line was needed are shown in Table 2.

We note the distribution of Seyfert 2s (Sy2s) and intermediate Seyfert types as defined in D. E. Osterbrock & G. J. Ferland (2006) and reported for these objects in K. Oh et al. (2022). Of the 71 objects classified as DPEs, 11 (15%) have BASS spectral types as Sy1s, 17 (24%) as Sy1.2s, 23 (32%) as Sy1.5s, six (8%) as Sy1.8s, and 14 (20%) as Sy1.9s.

 ${\bf Table~1} \\ {\bf Properties~of~the~70~DPE~Candidates~from~the~BASS~Broad-line~AGN~Sample}$

ID	R.A.	Decl.	z	Type	Galaxy Morphology	W2	W1 – W2	ZTF Variance	WISE	VLASS 3 GHz	RACS 1 GHz
(1)	(hh:mm:ss)	(dms)	(4)	(5)	(6)	(mag)	(mag)	(0)	χ^2/dof	(mJy)	(mJy)
(1)	(2)	(3)	(4)	(5)	(6)	(7)	(8)	(9)	(10)	(11)	(12)
45	01:01:24.38	-03:08:40.20	0.0696	Sy1.5	Disk-no-spiral	11.6	0.56	0.03	250.1	ND	D
61	01:13:50.09	-14:50:44.52	0.0527	Sy1.2	Merger	9.93	0.78	0.04	740.94	1.87 ± 0.26	58.56 ± 4.7
107	02:07:02.21	+29:30:46.08	0.1092	Sy1.9	Smooth	10.9	1.0	0.03	681.84	22.49 ± 0.8	•••
111	02:08:34.94	-17:39:34.92	0.129	Sy1.5	Pointlike	10.48	0.89	0.1	95.12	153.74 ± 0.5	44.22 ± 3.65
116	02:14:33.55	+00:46:00.12	0.0263	Sy1.2	Disk-spiral	9.73	0.44	0.13	973.47	4.0 ± 0.36	6.4 ± 1.2
121	02:22:06.34	+52:21:05.76	0.2	Sy1.2	Pointlike	11.2	1.05	0.12	287.63	2.8 ± 0.59	•••
122	02:22:35.21	+25:08:14.64	0.062	Sy1.5	Disk-spiral	10.27	0.82	0.01	456.02	2.53 ± 0.26	3.39 ± 0.86
136	02:38:19.73	-52:11:32.28	0.0456	Sy1	Smooth	10.08	0.77		8543.39	•••	2.76 ± 0.89
147	02:44:57.70	+62:28:06.60	0.0448	Sy1	Other/unc.	7.35	1.09	0.04	1004.02	645.11 ± 2.41	•••
162	03:00:04.32	-10:49:28.56	0.0328	Sy1.2	Disk-no-spiral	8.85	0.92	0.22	2696.59	8.84 ± 0.33	26.52 ± 2.62
166	03:10:44.38	+32:39:29.16	0.127	Sy1	Other/unc.	10.0	1.0		334.26	ND	
187	03:35:22.58	+19:07:28.92	0.189	Sy1.8	Pointlike	11.38	1.11		455.38	2.59 ± 0.3	5.88 ± 1.08
232	04:40:47.71	+27:39:46.80	0.0364	Sy1.5	Smooth	11.14	0.63	0.14	388.96	2.57 ± 0.26	6802.05 ± 478.02
236	04:43:46.80	+28:58:18.84	0.0215	Sy1.9	Other/unc.	9.86	0.74	0.11	2204.5	5.3 ± 0.26	D
270	05:19:49.73	-45:46:43.68	0.035	Sy1.2	Smooth	9.6	0.94		1061.23		D
315	06:00:40.10	+00:06:18.36	0.114	Sy1.9	Smooth	9.13	1.12	0.23	32.96	35.71 ± 0.31	2080.45 ± 147.2
367	07:23:53.04	-08:06:14.40	0.146	Sy1	Pointlike	11.72	0.87	0.13	146.07	ND	
372	07:27:21.12	-24:06:32.40	0.122	Sy1.5	Pointlike	10.16	1.12		20.75	11.73 ± 0.36	68.26 ± 5.48
381	07:43:01.44	+80:26:26.16	0.118	Sy1.9	Other/unc.	11.34	1.09	0.06	790.24	3.02 ± 0.38	
395	07:52:44.16	+45:56:57.48	0.051	Sy1.5	Smooth	11.06	0.33	0.1	254.47	39.39 ± 0.62	•••
413	08:18:14.64	+01:22:27.12	0.0894	Sy1.9	Disk-spiral	10.54	0.98	0.21	806.59	9.1 ± 0.27	3.48 ± 1.21
418	08:29:42.72	+41:54:36.72	0.1264	Sy1.5	Smooth	10.83	0.9	1.26	2450.27	4.33 ± 0.35	
420	08:32:25.44	+37:07:36.12	0.0922	Sy1.2	Smooth	10.37	1.02	0.08	2989.52	5.92 ± 0.24	

Note. Properties of the 71 DPE candidates identified among the BASS broad-line AGN. Column (1): Swift-BAT ID number from M. J. Koss et al. (2022a). Columns (2)–(3): R.A. and decl. of the BAT counterpart from M. J. Koss et al. (2022a). Column (4): spectroscopic redshift from M. J. Koss et al. (2022a). Column (5): Seyfert classification from K. Oh et al. (2022). Column (6): galaxy morphology classification from M. Parra Tello et al. (2025). Columns (7) and (8): median W2 Vega magnitude and median W1 – W2 color across the NEOWISE light curves. Column (9): excess variance from the *g*-band ZTF light curves. Column (10): χ^2 /dof of the WISE W2 light curves. Column (11): 2–4 GHz radio flux from VLASS for epoch 1 (2017–2018), with a 2″.5 beam, where ND indicates radio edge-on detection and dash indicates that the source was not within the surveyed region. Column (12): 1 GHz radio flux from ASKAP-RACS, with 15″ resolution, where D indicates that the source is visible in publicly available RACS imaging but is not in fields covered by the epoch 1 catalog.

(This table is available in its entirety in machine-readable form in the online article.)

 Table 2

 Best-fit Accretion Disk Parameters for 71 Objects Classified as DPEs

ID	Source	Date	ξ_1	ξ_2	σ	i	q	w	A_s	ψ	ϕ_0	BL?
					$(km s^{-1})$	(deg)		(deg)		(deg)	(deg)	
(1)	(2)	(3)	(4)	(5)	(6)	(7)	(8)	(9)	(10)	(11)	(12)	(13)
45	XSHO	2019-08-01	200^{+10}_{-10}	1310^{+290}_{-510}	1410^{+70}_{-60}	13^{+1}_{-1}	$2.4^{+0.1}_{-0.1}$	81+12	$0.9^{+0.1}_{-0.1}$	56+21	294^{+26}_{-29}	N
61	DBSP	2019-08-02	120^{+10}_{-10}	3120^{+20}_{-20}	930^{+90}_{-70}	17^{+1}_{-1}	$1.9^{+0.1}_{-0.1}$	86^{+5}_{-3}	$1.0^{+0.1}_{-0.1}$	26^{+16}_{-14}	221^{+350}_{-48}	N
107	ARCH	2018-08-24	360^{+30}_{-40}	1280^{+370}_{-560}	1580^{+50}_{-70}	21^{+1}_{-1}	$2.4^{+0.2}_{-0.1}$	44^{+12}_{-16}	$1.0^{+0.1}_{-0.1}$	51^{+89}_{-28}	336^{+14}_{-212}	N
111	DBSP	2019-08-23	260^{+20}_{-20}	3860^{+90}_{-100}	1670^{+50}_{-50}	22^{+1}_{-1}	$2.1^{+0.1}_{-0.1}$	89^{+2}_{-1}	$1.0^{+0.1}_{-0.1}$	65^{+18}_{-16}	294^{+18}_{-24}	N
116	XSHO	2017-12-05	220^{+10}_{-10}	3990^{+10}_{-10}	850^{+20}_{-20}	20^{+1}_{-1}	$2.2^{+0.1}_{-0.1}$	90^{+1}_{-1}	$1.0^{+0.1}_{-0.1}$	40^{+8}_{-7}	224^{+14}_{-11}	N
121	DBSP	2017-08-31	400^{+50}_{-80}	9730^{+400}_{-200}	1250^{+100}_{-110}	36^{+2}_{-4}	$14.4^{+1.8}_{-1.8}$	0_{-1}^{+1}	$14.8^{+4.7}_{-6.7}$	2^{+1}_{-1}	1^{+1}_{-1}	Y
122	DBSP	2016-10-02	240^{+50}_{-50}	3580^{+590}_{-320}	900^{+180}_{-230}	25^{+2}_{-2}	$1.8^{+0.3}_{-0.2}$	66^{+26}_{-17}	$0.8^{+0.3}_{-0.2}$	41^{+83}_{-33}	342^{+72}_{-202}	N
136	BNCH	2016-09-12	220^{+40}_{-40}	1200^{+220}_{-560}	1590^{+100}_{-90}	13^{+1}_{-1}	$1.9^{+0.7}_{-0.4}$	83^{+12}_{-5}	$0.9^{+0.1}_{-0.1}$	61^{+22}_{-21}	288^{+30}_{-27}	N
147	DBSP	2016-10-02	110^{+30}_{-30}	2030^{+260}_{-330}	2740^{+180}_{-140}	27^{+1}_{-2}	$1.5^{+0.1}_{-0.2}$	45^{+20}_{-26}	$0.8^{+0.3}_{-0.1}$	52^{+24}_{-25}	240^{+23}_{-51}	N
162	DBSP	2018-08-23	130^{+10}_{-10}	1010^{+60}_{-30}	600^{+30}_{-20}	13^{+1}_{-1}	$22.2_{-0.9}^{+1.0}$	1^{+1}_{-1}	$84.2^{+5.1}_{-4.2}$	20^{+1}_{-1}	8^{+1}_{-1}	Y
166	DBSP	2017-08-31	340^{+40}_{-40}	2570^{+160}_{-200}	1440^{+60}_{-70}	20^{+1}_{-1}	$8.2^{+0.8}_{-1.5}$	-0^{+1}_{-1}	$16.5^{+5.8}_{-6.6}$	4^{+1}_{-1}	3^{+1}_{-1}	N
187	LRIS	2019-12-24	60^{+10}_{-20}	9750^{+510}_{-190}	1370^{+110}_{-160}	28^{+1}_{-1}	$1.6^{+1.1}_{-1.8}$	-0^{+1}_{-1}	$15.0^{+0.7}_{-0.4}$	3^{+1}_{-1}	2^{+1}_{-1}	N
232	DBSP	2018-09-10	170^{+10}_{-10}	1200^{+200}_{-240}	1170^{+80}_{-70}	13^{+1}_{-1}	$2.4^{+0.1}_{-0.1}$	81^{+11}_{-6}	$0.9^{+0.1}_{-0.1}$	59^{+22}_{-22}	291^{+26}_{-26}	N
236	DBSP	2017-08-31	680^{+360}_{-180}	860^{+140}_{-110}	1410^{+100}_{-80}	16^{+1}_{-1}	$1.8^{+0.5}_{-0.5}$	86^{+6}_{-3}	$9.6^{+0.4}_{-0.3}$	30^{+47}_{-50}	259^{+8}_{-7}	N
270	BNCH	2016-09-11	1130^{+470}_{-600}	4000^{+10}_{-10}	2630^{+320}_{-220}	57^{+13}_{-23}	$1.8^{+0.6}_{-0.5}$	45^{+31}_{-31}	$0.5^{+0.4}_{-0.3}$	7^{+35}_{-36}	108^{+578}_{-672}	N
315	MAGE	2019-12-10	270^{+110}_{-20}	590^{+20}_{-20}	2000^{+10}_{-80}	24^{+2}_{-1}	$25.5^{+0.3}_{-0.4}$	-0^{+1}_{-1}	$40.7^{+0.4}_{-0.3}$	5^{+1}_{-1}	7^{+1}_{-1}	Y
367	DBSP	2018-03-28	340^{+150}_{-230}	1900^{+10}_{-10}	1590^{+40}_{-60}	28^{+3}_{-3}	$1.2^{+0.3}_{-0.7}$	56^{+22}_{-24}	$6.8^{+3.1}_{-2.3}$	28^{+76}_{-40}	341^{+101}_{-224}	N
372	XSHO	2019-03-19	820^{+40}_{-50}	4000^{+10}_{-10}	1570^{+30}_{-10}	53^{+2}_{-2}	$2.5^{+0.1}_{-0.1}$	26^{+5}_{-9}	$9.2^{+1.1}_{-0.6}$	57^{+22}_{-21}	167^{+17}_{-30}	N
381	DBSP	2016-01-12	1040^{+850}_{-700}	3490^{+740}_{-370}	2190^{+700}_{-440}	26^{+5}_{-5}	$1.5^{+0.5}_{-0.6}$	47^{+33}_{-30}	$0.5^{+0.4}_{-0.3}$	41^{+68}_{-30}	287^{+79}_{-62}	N
395	SDSS	2004-02-20	240^{+60}_{-90}	3990^{+10}_{-10}	3000^{+10}_{-10}	19^{+2}_{-5}	$2.5^{+0.1}_{-0.1}$	78^{+21}_{-8}	$4.8^{+1.7}_{-1.9}$	14^{+1}_{-2}	175^{+37}_{-22}	Y
413	BNCH	2017-10-02	260^{+130}_{-380}	2950^{+10}_{-10}	2410^{+40}_{-50}	88^{+218}_{-181}	$1.6^{+0.5}_{-0.5}$	51^{+33}_{-28}	$5.8^{+3.4}_{-3.3}$	3^{+61}_{-63}	11^{+467}_{-468}	N
418	SDSS	2001-12-23	150^{+10}_{-10}	3900^{+50}_{-40}	2640^{+140}_{-150}	8^{+2}_{-1}	$2.5^{+0.1}_{-0.1}$	60^{+34}_{-22}	$0.8^{+0.5}_{-0.2}$	24^{+77}_{-46}	218^{+495}_{-580}	N
420	SDSS	2002-02-07	50^{+10}_{-10}	1590^{+40}_{-50}	720^{+460}_{-30}	27^{+1}_{-1}	$35.4^{+0.9}_{-0.6}$	-0^{+1}_{-2}	$98.8^{+15.2}_{-1.9}$	8^{+1}_{-1}	27^{+1}_{-1}	Y

Note. Best-fit disk parameters from modeling the broad H α line of the AGN with the circular accretion disk model from K. Chen & J. P. Halpern (1989) and with an additional spiral arm superposed (J. S. Schimoia et al. 2017). Column (1): Swift-BAT ID. Column (2): instrument used for observation (K. Oh et al. 2022); Column (3): date of observation; Column (4): radius ξ_1 (gravitational radii); Column (5): outer radius ξ_2 (gravitational radii); Column (6): turbulent broadening σ (km s⁻¹); Column (7): inclination angle i (deg); Column (8): spiral arm width w (deg); Column (9): spiral arm amplitude expressed as contrast ratio A_s ; Column (10): spiral arm pitch angle ψ (deg); Column (11): spiral arm phase ϕ_0 (deg); Column (12): additional Gaussian broad line was fitted (Y/N).

(This table is available in its entirety in machine-readable form in the online article.)

When looking at the total sample of 343 AGN, 11 of 47 Sy1s were DPEs (23%), 17 of 84 Sy1.2s were DPEs (20%), 23 of 137 Sy1.5s were DPEs (17%), six of 36 Sy1.8s were DPEs (17%), and 14 of 52 Sy1.9s were DPEs (27%).

We note that a subset of the objects in Table 1 has been previously identified as DPEs. BAT 107 (3C 59), BAT 473 (3C 277), BAT 800 (3C 332), BAT 907 (PKS 1739+18C), BAT 994 (3C 390.3) were reported in M. Eracleous & J. P. Halpern (1994). BAT 270 (Pictor A) and BAT 420 (CBS 74) were reported in M. Eracleous & J. P. Halpern (2003). BAT 443 (J090436) and BAT 1183 (J230443) were reported as DPEs in I. V. Strateva et al. (2003). For the five objects with circular disk model parameters reported from spectra taken in 1991-1998 in M. Eracleous & J. P. Halpern (1994) and M. Eracleous & J. P. Halpern (2003) (BAT 107, BAT 800, BAT 994, BAT 270, and BAT 420), inclination angles reported from the fits to BASS spectra are consistent with previous fits within 3σ uncertainties, and have comparable estimates of the inner and outer radii. We note that the small differences observed in some parameters can arise naturally from small changes to the observed profile shape and the slightly different modeling approach, where we allow a small amplitude spiral arm to improve the fit.

While there are no significant changes in the peak separations for the 5 objects when comparing the 1991–1998 spectra to the BASS spectra taken three decades later, we note

that BAT 800 and BAT 994 both show an increase in the flux of the broad-line profile compared to the narrow emission lines, and BAT 994 shows an increase in the blue-to-red shoulder flux ratio, consistent with year-to-decade evolution observed in samples of DPEs in J. S. Schimoia et al. (2017) and C. Ward et al. (2024). BAT 420 does not exhibit a major change in the disk profile except for adding a broad bump blueward of the blue shoulder in the disk profile.

3. Variability of the Properties of BASS DPEs and Other Broad-line AGN

Motivated by previous studies suggesting (a) a high fraction of DPEs among optically variable AGN (C. Ward et al. 2024) and (b) different turnover frequencies between DPEs and other broad-line AGN (X.-G. Zhang & L.-L. Feng 2017), we make a comparison of the level of optical and mid-IR variability of the two populations. We constructed optical light curves of the BASS DPEs and non-DPE broad-line AGN sample from ZTF *g*- and *r*-band imaging using the ZTF forced photometry service, which produces point-spread function photometry from the ZTF difference images (F. J. Masci et al. 2019). We extracted all available photometry from the ZTF public and partnership fields between 2018 January 1 and 2024 March 1. After removing poor quality images by requiring the procstatus flag be = 0, we measured the baseline flux

 Table 3

 Comparison of DPEs and the Non-DPE Broad-line AGN Sample for Various Multiwavelength Quantities

Quantity (1)	# DPEs (2)	# Non-DPEs (3)	DPE Median (4)	Non-DPE Median (5)	KS Statistic (6)	<i>p</i> -value (7)
W1 – W2 (Vega mag)	70	280	0.88 ± 0.27	0.85 ± 0.26	0.08	0.827
WISE W2 excess variance (Vega mag.)	70	280	-0.00 ± 0.03	-0.01 ± 0.04	0.16	0.104
WISE W2 χ^2 variance (Vega mag)	70	280	338.97 ± 1311.55	403.23 ± 908.79	0.09	0.700
ZTF g-band excess variance (AB mag)	58	207	0.10 ± 0.26	0.13 ± 0.45	0.11	0.612
$nH (cm^{-2})$	66	278	20.70 ± 1.17	20.70 ± 1.33	0.07	0.921
$\alpha_{ m ox}$	28	138	-1.31 ± 0.20	-1.28 ± 0.20	0.11	0.928
Si VI line luminosity	3	28	39.83 ± 0.69	40.22 ± 0.74	0.38	0.709
Fe K α EW (eV)	18	67	136.00 ± 331.80	126.00 ± 239.20	0.13	0.949
Fe K α energy (erg s ⁻¹)	18	67	6.39 ± 0.30	6.41 ± 0.11	0.31	0.111
$\log(L_{ m bHeta}/L_{ m bHlpha})$	41	196	-0.63 ± 0.29	-0.57 ± 0.44	0.19	0.148
$\log M_{ m BH}(M_{\odot})$	18	85	8.18 ± 0.45	7.80 ± 0.58	0.39	0.015
$L_{3 \text{ GHz}} \text{ (erg s}^{-1}\text{)}$	52	176	29.53 ± 1.16	29.43 ± 1.08	0.14	0.344
$L_{22 \text{ GHz}} \text{ (erg s}^{-1}\text{)}$	14	95	38.35 ± 1.14	38.03 ± 0.65	0.31	0.143
$L_{1 \text{ GHz}} \text{ (erg s}^{-1}\text{)}$	28	140	38.33 ± 1.29	38.16 ± 1.08	0.27	0.056
$L_{2-10 \text{ keV}} \text{ (erg s}^{-1})$	55	216	43.79 ± 0.77	43.32 ± 0.87	0.29	0.001
$\log L/L_{ m Edd}$	17	81	-1.87 ± 0.60	-1.56 ± 0.58	0.32	0.075
O IB/H α	71	285	0.08 ± 0.09	0.05 ± 3.26	0.31	0.000020
S IIB/H α	71	285	0.25 ± 0.17	0.22 ± 329.63	0.11	0.471
N IIb/Hα	71	285	0.19 ± 0.16	0.20 ± 11737.19	0.08	0.778
O IIIb/H β	71	285	7.56 ± 4.24	6.78 ± 4715.37	0.13	0.240

Note. Comparison of multiwavelength properties of the BASS DPE sample and the sample of non-DPE broad-line AGN. Column (1): quantity being compared and units for quoted medians. Columns (2)–(3): number of DPEs and non-DPE broad-line AGN, respectively, with a measurement of that quantity. Column (4): median and standard deviation for the DPE sample. Column (5): median and standard deviation for the non-DPE sample. Column (6): two-sample KS statistic. Column (7): p-value for the probability with which we can reject the null hypothesis that the non-DPE broad-line AGN and DPE parameters are drawn from the same distributions.

(This table is available in its entirety in machine-readable form in the online article.)

from the reference images, applied zero-points, and combined the baseline flux measured from the reference images and the single-epoch fluxes to produce g- and r-band light curves of the two samples. We also produced mid-IR photometry available in W1 (3.4 μ m) and W2 (4.6 μ m) bands from the WISE mission (A. Mainzer et al. 2011, 2014). We obtained the NEOWISE light curves from IRSA (NEOWISE Team 2020). NEOWISE observes each field with a \sim 6 month cadence, taking multiple observations over a short < 2 day period. We report the median and standard deviation of the observations taken upon each \sim 6 monthly visit to the field. The mid-IR light curves of selected DPEs are also shown in Figure 5.

In order to quantify the level of optical variability to facilitate comparison between DPEs and the non-DPE broadline AGN sample, we calculated the excess variance of the ZTF g-band light curves, given by $\sigma_{\rm NXS}^2 = \frac{S^2 - \sigma_n^2}{\bar{f}^2}$, where \overline{f} is the mean flux, S^2 is the total variance of the light curve, and σ_n^2 is the mean square photometric error associated with each measured flux (F. Vagnetti et al. 2011). We note that the galaxy light contribution is included in the reported light curves via the addition of the reference image flux to the difference image fluxes, but our variability statistics capture the level of variability relative to the mean and will not be affected by the galaxy light contribution. For the WISE W2 light curves, we report the $\chi^2/{\rm dof}$ for a constant light curve at the median flux value, which was found to quantify AGN-like variability well in S. van Velzen et al. (2021), with χ^2 dof > 10 being a good indicator of AGN-like long-term variability. Table 1 reports the optical and mid-IR variability metrics. The W2 χ^2 /dof distributions and g-band excess variance are shown in Figures 6(a) and (b). We applied a two-sample Kolmogorov–Smirnov (KS) test to both parameters to determine the probability with which we can reject the null hypothesis that the non-DPE broad-line AGN and DPE parameters were drawn from the same distributions. For the optical excess variance and mid-IR χ^2 /dof, we obtain p-values of 0.61 and 0.70, indicating that we do not have evidence that they were drawn from different distributions (Table 3). All AGN in both populations are variable in the optical and mid-IR.

4. Comparing Multiwavelength Properties of BASS DPEs and Non-DPE Broad-line AGN

To determine if the X-ray properties of the two samples differed, we compared the intrinsic X-ray luminosity $\log L_{2-10\,\mathrm{keV}}$ (erg s⁻¹) and the column density of the neutral obscuring material derived from broadband X-ray spectra $N_{\rm H}$, both reported in C. Ricci et al. (2017). We find that the DPE population tends to be more X-ray luminous, with DPEs having a median and standard deviation $\log L_{2-10 \,\mathrm{keV}}$ (erg s⁻¹) of 43.79 ± 0.77 and non-DPEs having a median and standard deviation $\log L_{2-10\,\mathrm{keV}}$ (erg s⁻¹) of 43.32 ± 0.87 . While each population has a broad range of $\log L_{2-10 \, \mathrm{keV}}$ (erg s⁻¹) values, a KS test to determine if the two samples have luminosities drawn from different distributions yielded a p-value of 0.001 (Figure 6(c), Table 3). Comparison of the $N_{\rm H}$ values, however, does not find any differences in the level of obscuring gas along the line of sight between the two populations (Figure 6(d), Table 3). We also compare the Balmer decrement derived from the broad-line luminosities obtained from multi-Gaussian fitting by J. E. Mejía-Restrepo et al. (2022) in order

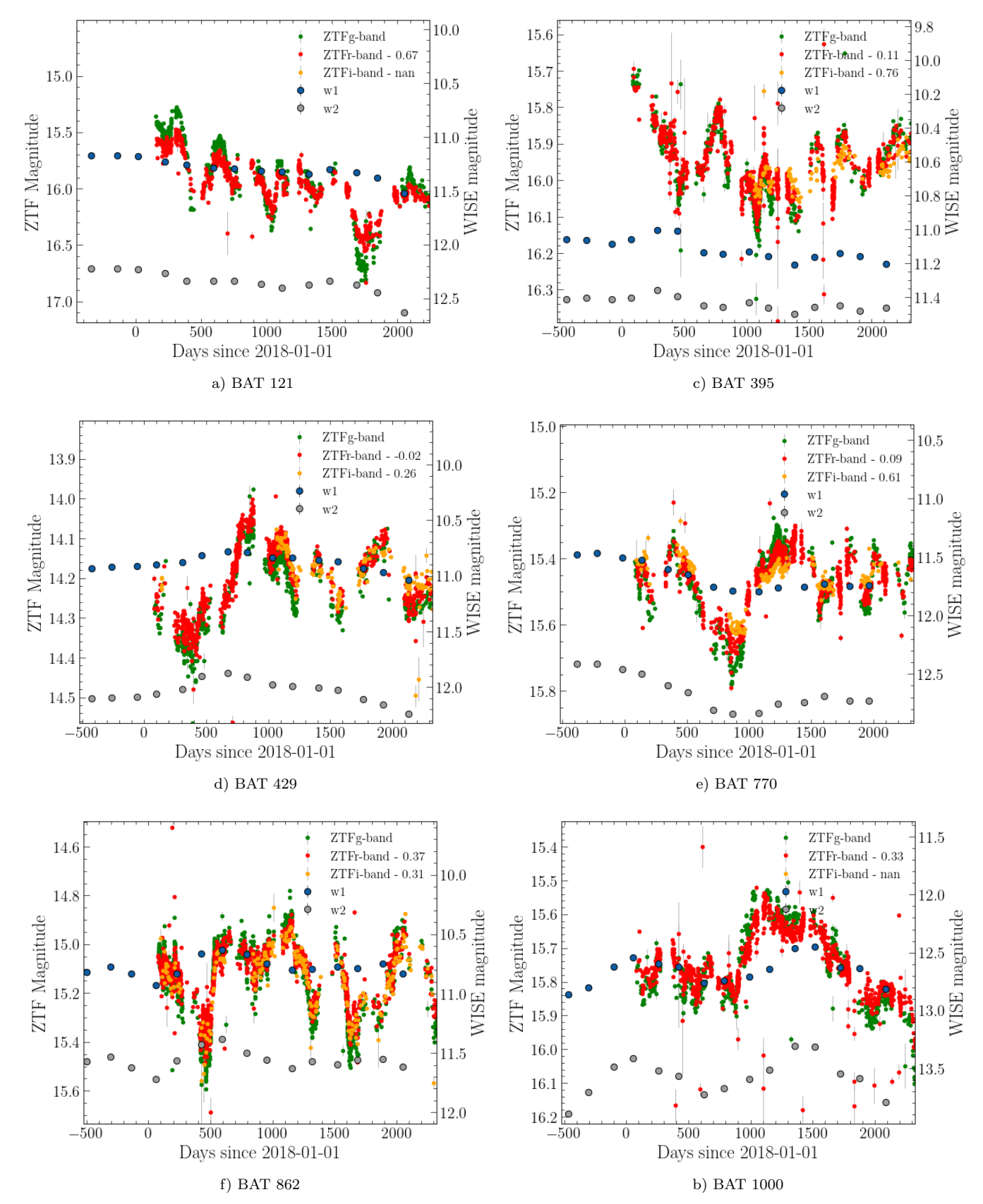


Figure 5. Optical (ZTF) and mid-IR (WISE) light curves of six BASS DPEs. The left y-axes display the ZTF AB magnitudes, while the right y-axes display the WISE Vega magnitudes.

to search for differences in the physical conditions of the BLR dust, such as the density. DPEs have a slightly smaller $\log L_{\rm bH\beta}/L_{\rm bH\,\alpha}$ by 0.13 dex, but we cannot exclude that they

are drawn from the same population with a KS test (Figure 6(e), Table 3). We note that uncertainties in the ${\rm H}\alpha$ and ${\rm H}\beta$ fluxes due to flux calibration issues reported in

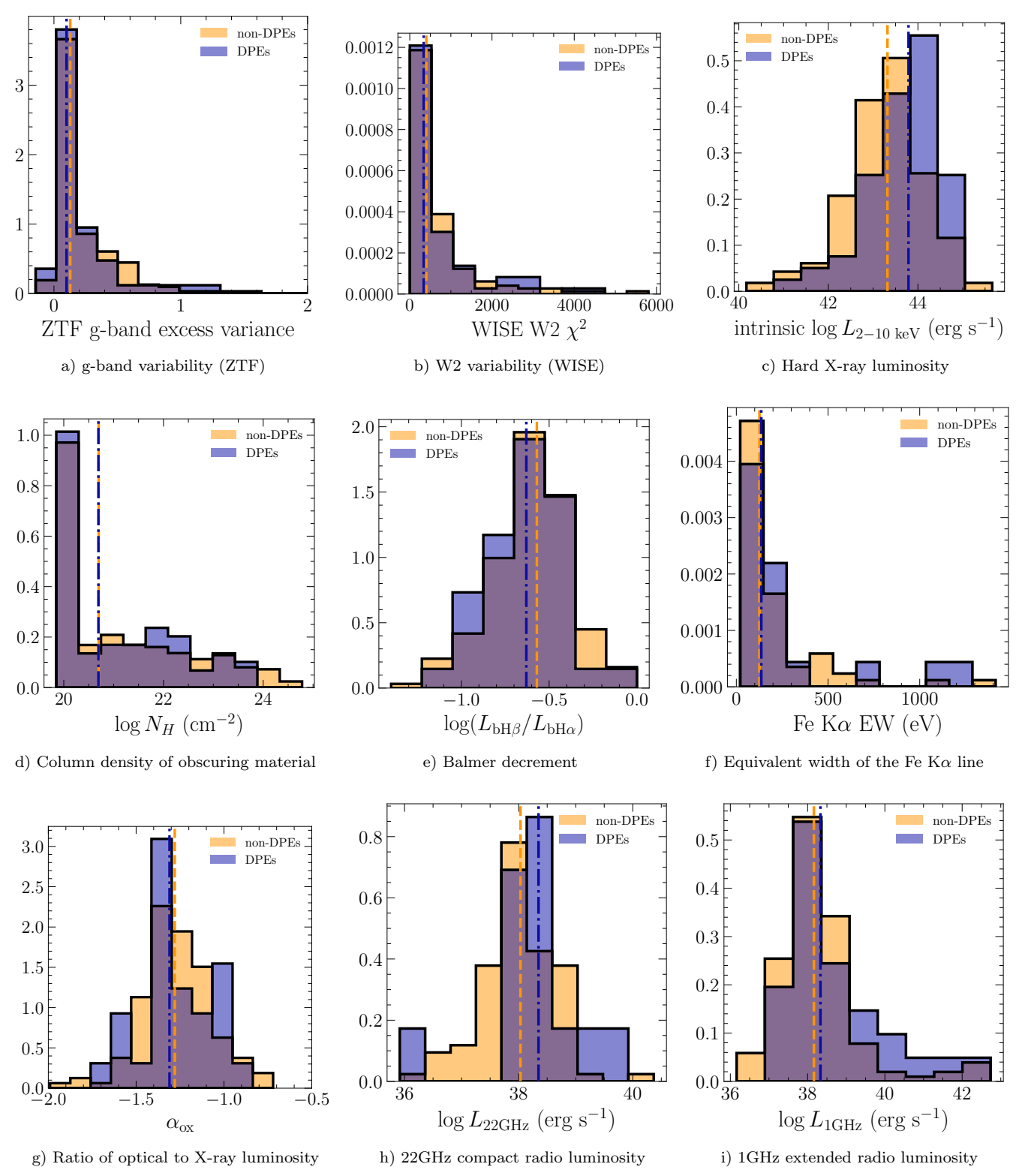


Figure 6. Normalized histograms comparing multiwavelength properties of the BASS AGN after they are split into two classes: DPEs and non-DPE broad-line BASS AGN. For each histogram, we only show cases where that property was detected. The number of objects with detections going into each histogram is indicated in Table 3. We indicate the median of each sample with a vertical purple dotted—dashed line (DPEs) and an orange dashed line (non-DPEs).

J. E. Mejía-Restrepo et al. (2022) may mean we have artificial biases in the reported Balmer decrements.

We include a comparison of the equivalent widths and energies of the Fe K α lines derived from X-ray spectroscopy analysis reported in C. Ricci et al. (2017). The DPEs have Fe K α line energies and equivalent widths (EWs) which are

typical of the BASS AGN sample as a whole (Table 3, Figure 6(f) for EWs). We also show the distributions in the optical to X-ray flux ratio $\alpha_{\rm ox}$ reported for this population in K. K. Gupta et al. (2024). We do not find any associations between DPEs and the X-ray/optical luminosity ratio (Figure 6(g), Table 3).

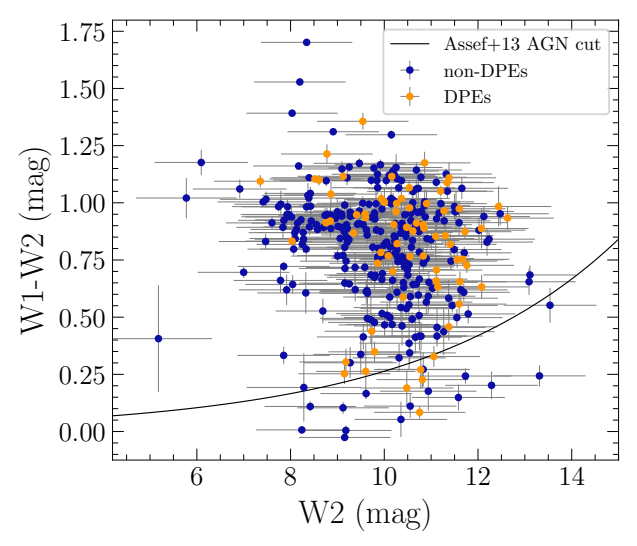


Figure 7. W1 — W2 color vs. W2 magnitude, and the R. J. Assef et al. (2013) cutoff for AGN. Magnitudes are Vega magnitudes. We show the BASS AGN split into two samples: DPEs and non-DPE BASS broad-line AGN.

We compared the 22 GHz radio luminosities from the galaxy nucleus measured from 1" resolution Very Large Array imaging (M. Magno et al. 2025). The distribution of $L_{22\rm GHz}$ of the DPEs and non-DPE broad-line AGN with associated radio emission is shown in Figure 6(h). The DPEs had a slightly higher median by 0.32; however, a two-sample KS test comparing the radio luminosities of the two populations has a p-value of 0.31, so we cannot rule out that they are from the same distribution for the 14 DPEs and 95 non-DPEs with 22 GHz imaging (Table 3).

We also compared the 3 GHz radio luminosities for all targets that were observed in the Karl G. Jansky Very Large Array Sky Survey at 2".5 resolution (VLASS; M. Lacy et al. 2020). We searched for crossmatches within 10" in Table 2 of the VLASS Epoch 1 Quick Look Catalogs, which contains ~700,000 compact radio sources with >1 mJy beam⁻¹ detections associated with mid-IR hosts from the unWISE catalog (Y. A. Gordon et al. 2021). Out of the 65 DPEs in the VLASS survey area, 52 (80%) had compact radio sources in VLASS. By comparison, for the broad-line AGN that were classified as non-DPEs, 166 out of 235 (71%) were detected in VLASS. A two-sample KS test comparing the radio luminosities of the two populations has a *p*-value of 0.34, indicating no clear difference between the populations at 3 GHz (Table 3).

We also searched for radio emission in the Rapid ASKAP Continuum Survey (RACS), with first epoch observations covering the whole southern sky to +41 deg decl. with the Australia Square Kilometre Array Pathfinder at a central wavelength of 887.5 MHz at 15" resolution (C. L. Hale et al. 2021). We crossmatched our sample with a 10" radius to the first Stokes I Source Catalog Data Release, which has an estimated 95% point source completeness at an integrated flux density of ~3 mJy. For any sources within the fields covered by the first data release that did not have a reported detection, we inspected imaging around the source coordinates with the CIRADA Image Cutout Web Service. For all observed sources without a reported detection in the catalog, an extended radio structure was clear in the CIRIDA imaging.

Those sources are reported as detected at 1 GHz, but we do not report a flux in Table 1. All DPEs except for BAT 1104 and all non-DPE broad-line AGN had radio sources in low-resolution RACS imaging when available. DPEs were more likely to have high 1 GHz luminosities in the $\log L_{22~\rm GHz}$ (erg s⁻¹) = 39–43 range in low-resolution 1 GHz imaging, although we once again do not find strong evidence that they were not drawn from the same distribution, with the KS test *p*-value being 0.27 (Figure 6(i), Table 3).

We also compare the mid-IR flux and colors of the two populations, using the median values and standard deviations of the W1 and W2 light curves described in Section 3. The distributions of the DPEs and the non-DPE broad-line AGN sample in the WISE W1 – W2 versus W2 plot, with the classical AGN mid-IR color cut from R. J. Assef et al. (2013) overlaid, are shown in Figure 7. The majority of both samples are classified as AGN on this plot, and no significant differences in the WISE color of the two populations are found (Table 3).

We compare the narrow emission line ratios reported in K. Oh et al. (2022) on three Baldwin–Phillips–Telervich (BPT) diagrams (J. A. Baldwin et al. 1981) in Figure 8. We compare four line ratios for the two populations: the [O III] $\lambda 5007/H\beta$ ratio, the [N II] $\lambda 6583/H\alpha$ ratio, the [S II] $\lambda 6732/H\alpha$ ratio, and the [O I] $\lambda 6306/H\alpha$ ratio. The two-sample KS tests found evidence for differences between the two populations for the [O I] $\lambda 6306/\text{H}\alpha$ ratio with a p-value of 2×10^{-5} . The median [O I] $\lambda 6306/H\alpha$ ratio is ~ 0.3 dex greater for the DPE sample compared to the non-DPE sample. We discuss this further in Section 7. We note that for DPEs, the dip in the center of the $H\alpha$ and $H\beta$ broad-line profiles can mean that the line ratios are inflated if the broad lines are modeled as Gaussians. This may account for the differences in the ionization ratios between the two populations derived in K. Oh et al. (2022). We also compared the Si[VI] emission line detection fractions and luminosities measured in J. S. den Brok et al. (2022), as this emission line is not contaminated by any broad double-peaked profiles. For the 23 BASS AGN with disk profile fits and Si [V I] line measurements, there were no differences between the DPEs and the non-DPE broad-line AGN sample, with 50% of each subsample having emission lines, and with similar luminosity distributions between the two populations for those detected lines (Table 3).

5. BH Masses of DPEs and Non-DPE Broad-line AGN

By assuming virialized gas when deriving masses from the width of H α and H β broad-line profiles, virial masses will be overestimated for DPEs (M. Eracleous & J. P. Halpern 2003). We therefore must rely on extrapolations of BH mass from host stellar mass to identify if there are any intrinsic differences between the masses of DPEs and other broad-line AGN. We compared the BH masses derived from the stellar velocity dispersion of the host galaxies reported in T. Caglar et al. (2023) and applied the canonical J. Kormendy & L. C. Ho (2013) $M_{\rm BH}$ – σ_* for the two samples. We find a significant preference for DPEs with higher mass BHs, with DPEs having a median mass of $\log(M/M_{\odot}) = 8.2$ and the non-DPEs having a median mass of $log(M/M_{\odot}) = 7.8$ (Figure 9, Table 3). We also show the Eddington ratios derived from X-ray luminosity in C. Ricci et al. (2017) and BH mass inferred from stellar velocity dispersions in Figure 9. The median DPE $\log L/L_{\rm Edd}$ is lower by 0.31.

²⁵ http://cutouts.cirada.ca/

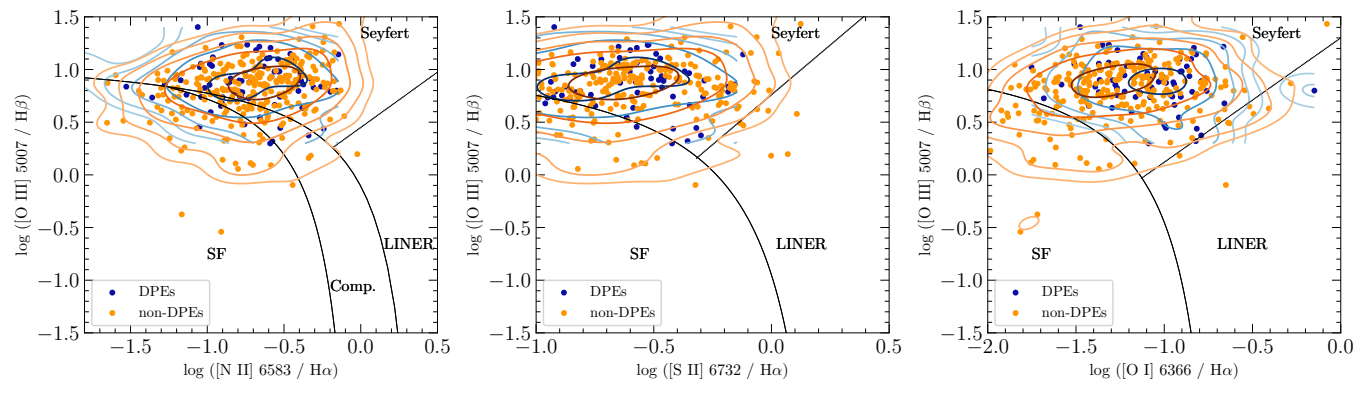


Figure 8. BPT diagrams showing the narrow emission line ratios derived in K. Oh et al. (2022) for BASS AGN split into two samples: DPEs and other broad-line AGN. The line diagnostics for different emission types (J. A. Baldwin et al. 1981; L. J. Kewley et al. 2001, 2006; G. Kauffmann et al. 2003; K. Schawinski et al. 2007) are shown with black lines.

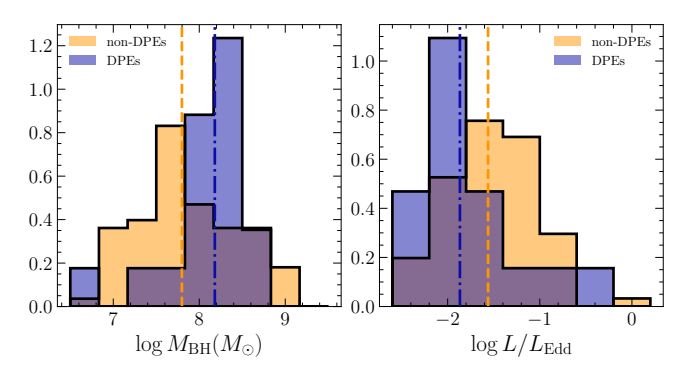


Figure 9. Comparison of masses (left) and derived Eddington ratios (right) when comparing DPEs and the non-DPE BASS broad-line AGN. For both the masses and the Eddington ratios we used the BH mass extrapolated from the stellar velocity dispersion of the host galaxy. We indicate the median of each sample with a vertical purple dotted–dashed line (DPEs) and an orange dashed line (non-DPEs).

In order to investigate how possible biases in virial mass measurements based on DPE broad-line profiles may introduce scatter in the the $M_{\rm BH}$ – σ_* , we show where DPEs and other BASS broad-line AGN lie on the relation when using virial measurements from J. E. Mejía-Restrepo et al. (2022) and stellar velocity dispersion from T. Caglar et al. (2023) (Figure 10). Aside from the clear preference for larger BH masses, the DPEs do not stand out from the BASS AGN, which already show a preference for low virial masses, typically falling within or below the nominal 0.3 dex scatter observed about the J. Kormendy & L. C. Ho (2013) relation.

6. Host Galaxy Properties

In order to compare the host galaxy properties of the DPEs to the other BASS AGN, we first generated a subsample of the main non-DPE broad-line AGN sample with comparable stellar mass and redshift to the DPEs. To do this, we used the host galaxy *i*-band magnitude reported in M. Parra Tello et al. (2025) and undertook a sampling procedure to obtain a subsample of the non-DPE broad-line AGN with the same *i*-band host magnitude distribution as the DPE hosts. The sampling procedure was as follows: for each sample, we select a DPE at random, and then we randomly select one of the 15 non-DPE broad-line AGN with *i*-band magnitudes closest to that DPE's *i*-band magnitude. We repeated this procedure 300 times to produce a control sample of 300 AGN. We confirmed

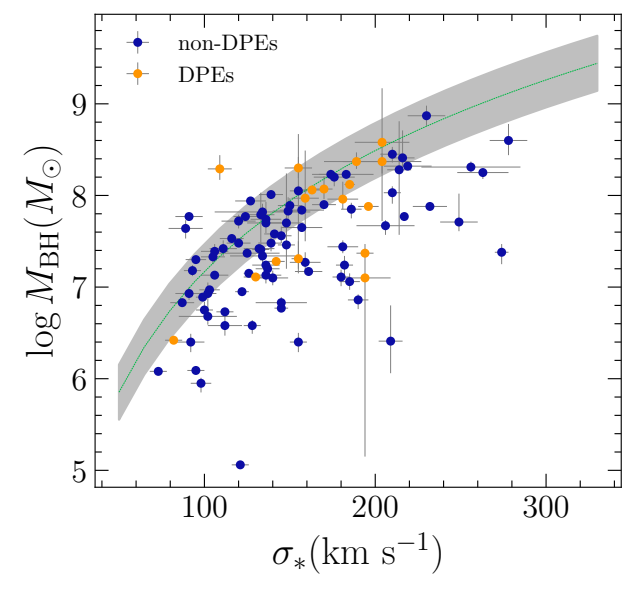


Figure 10. $M_{\rm BH}$ – σ_* relation for BASS AGN with virial mass measurements (J. E. Mejía-Restrepo et al. 2022) and stellar velocity dispersion measurements (T. Caglar et al. 2023). The canonical relation from J. Kormendy & L. C. Ho (2013) with a scatter of 0.3 dex is shown in gray.

that this sample had comparable distributions of redshift, mass, and *i*-band magnitude as the DPE sample.

We then compared the galaxy morphology classifications of the DPE sample and the *i*-band matched control sample, using the galaxy classifications reported in M. Parra Tello et al. (2025). We found that 33 of 71 DPEs (46%) are classified as having "smooth" (elliptical) morphologies compared to the control sample's 48 of 164 (31% \pm 2%), six of 71 DPEs (8%) are in mergers compared to the control sample's 28 of 164 (16 \pm 1%), and 10 of 71 (14%) DPEs are in "disk" galaxies—with or without a spiral—compared to the control sample's 43 of 164 (29% \pm 2%). The population fractions and their 1 σ uncertainties reported for the control sample are derived from repeating the procedure to generate the control sample 20 times, and taking the mean and standard deviation of the population fraction each time. We discuss this further in Section 7.

7. Discussion

Our lower limit of a 21% incidence rate of DPEs among BASS X-ray—selected AGN of Seyfert types 1–1.9 is

consistent with the detection rates previously found for a smaller sample of radio-loud broad-line AGN (M. Eracleous & J. P. Halpern 2003), and the 19% detection rate of DPEs among populations of optically variable broad-line AGN (C. Ward et al. 2021). It is substantially larger than the 3.6% observed in a sample of SDSS quasars identified in optical spectroscopy (I. V. Strateva et al. 2003).

Compared to the broad-line AGN sample, the low Eddington ratios and higher $[O I]/H\alpha$ line ratios are consistent with previous findings from smaller DPE populations (M. Eracleous & J. P. Halpern 2003). These findings have been explained by the expected spectral energy distribution (SED) of hot, vertically extended, optically thin, and radiatively inefficient accretion flow that can sustain radio jets and is more likely to appear at low-accretion rates: the SED of such an accretion flow is relatively hard, having a power law shape across UV and soft X-ray bands with a peak in the far-IR, and lacking a UV bump (T. Di Matteo et al. 1999, 2000; G. H. Ball et al. 2001). Such an ionizing continuum could produce the low ionization state of DPEs (T. Nagao et al. 2002; M. Eracleous & J. P. Halpern 2003). This supports a model that involves a transition in the BLR geometry to the observed disk-dominated state to produce such an SED.

We confirm that DPEs have a preference for elliptical galaxies (46% compared to an i-band magnitude-matched control sample's 31%), consistent with previous findings from M. Eracleous & J. P. Halpern (2003). We confirm that DPEs tend to have host galaxies with larger stellar velocity dispersions. It has previously been suggested that the high BH masses of DPEs may explain the high radio-loudness fraction: more massive BHs tend to be associated with smooth/elliptical galaxies (M. Eracleous & J. P. Halpern 2003; I. V. Strateva et al. 2003). However, in this sample, we find that all DPEs except for one and all non-DPE broad-line BASS AGN that have low-resolution RACS imaging available are detected at 1 GHz, and that a greater fraction of the population has high 1 GHz integrated luminosities in the $\log L = 39-43 \text{ erg s}^{-1}$ range than the non-DPEs. The DPEs in the sample had a slightly higher detection fraction in VLASS 3 GHz imaging (80% instead of 71% in the non-DPE sample), and did not have evidence for a difference in their 3 GHz luminosity distribution. When comparing compact 22 GHz compact emission in the 1" nuclear region, DPEs tend to have slightly higher luminosities by ~ 0.3 dex. We note that the equivalent widths of the Fe K α lines are known to correlate with X-ray luminosity, radio-loudness, and Eddington ratio (K. L. Page et al. 2004; P. Jiang et al. 2006), and in such cases, there is no evidence for a difference between disk emitters and the non-DPE broad-line AGN sample.

Given the higher $[O\,I]/H\alpha$ line ratios and possible association with a radiatively inefficient accretion flow that could sustain radio jets, it is surprising that we do not see a stronger preference for DPEs to have higher radio detection rates and luminosities in the various radio analyses. Y. Terashima & A. S. Wilson (2003) previously found that the X-ray to radio luminosity ratio was able to produce a strong separation between Seyferts and low-luminosity AGN. In order to investigate whether DPEs show a preference for low $L_{\rm X}$ to $L_{\rm R}$ values, we plot the compact 22 GHz radio luminosity from M. Magno et al. (2025) against the 2–10 keV X-ray luminosity of the two classes in Figure 11. We overlay

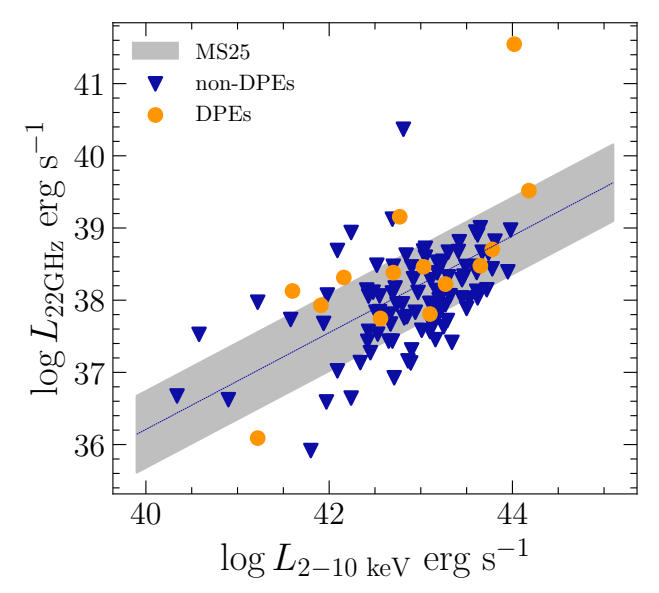


Figure 11. Compact 22 GHz radio luminosity from M. Magno et al. (2025) vs. the 2–10 keV X-ray luminosity reported in C. Ricci et al. (2017) for DPEs and non-DPE broad-line BASS AGN. In gray, we show the best-fit relation for BASS radio-detected AGN from M. Magno et al. (2025). No strong separation is seen between the two populations.

the best-fit relation found for the BASS AGN in gray, which was found by M. Magno et al. (2025) to be consistent with an extension of the relation found for coronally active stars (M. Guedel & A. O. Benz 1993) that extrapolates well to radio-quiet quasars (A. Laor & E. Behar 2008). We note that both the DPEs and non-DPE BASS AGN are primarily radioquiet, with the exception of one DPE and one non-DPE AGN with 22 GHz luminosities greater than 40 erg s⁻¹, which are classified as radio-loud (M. Magno et al. 2025). We do not see separate clusters associated with the non-DPE broad-line AGN/DPE subclasses, and coronae are the primary drivers of compact 22 GHz emission in both populations. According to the predictions of the disk-wind model of M. Elitzur & L. C. Ho (2009), M. Elitzur et al. (2014), DPEs would be expected to preferentially appear in intermediate-type Seyferts over Sy1s. This is because at lower accretion rates, more gas is expected to shift from high-altitude trajectories along the wind streamlines to low-altitude motion that follows the disk motion, causing a decrease in flux of single-peaked broadline emission associated with winds and an increase in flux of a double-peaked disk emission line profile. Among our sample, 11 of 47 Sy1s were DPEs (23%), 17 of 84 Sy1.2s were DPEs (20%), 23 of 137 Sy1.5s were DPEs (17%), six of 36 Sy1.8s were DPEs (17%), and 14 of 52 Sy1.9s were DPEs (27%). We therefore do not see strong correlations between DPE fraction and the broad-to-narrow-line ratio in this systematically classified sample of AGN.

In Figure 12, we show where the BASS AGN lie on the $L_{\rm bol}$ versus $M_{\rm BH}$ relation using the BH masses derived from stellar velocity dispersions and the bolometric luminosities derived from intrinsic luminosity in the 14–150 keV ranges (C. Ricci et al. 2017; M. J. Koss et al. 2022a). We also show the boundary where the BLR emission is expected to disappear as the low radiative efficiency results in an advection-dominated state such that the BLR cannot be sustained (M. Elitzur & L. C. Ho 2009). The BASS sample, including Sy2s shown in Figure 12, does not reach sufficiently low luminosities to enter

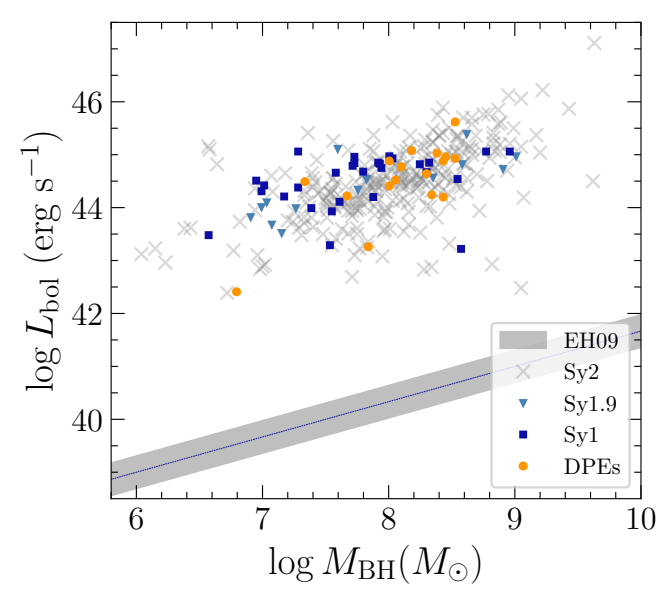


Figure 12. AGN bolometric luminosity derived from X-ray luminosity vs. BH mass estimated from stellar velocity dispersions of host galaxies for four subsamples of the BASS AGN: DPEs, Sy2s, and Sy1.9s that did not pass the DPE criteria, and the BASS Sy2 sample. The black line denotes the M. Elitzur & L. C. Ho (2009) critical luminosity boundary expected to be the threshold below which the BLR disappears in the disk-wind model, while the gray shaded error region denotes a range of 0.3 dex based on typical scatter in bolometric luminosities derived from X-ray luminosities (L. C. Ho 2009).

this boundary region where M. Elitzur & L. C. Ho (2009) and M. Elitzur et al. (2014) observe only Sy2s and no broad-line AGN for the Palomar spectroscopic survey AGN sample. However, we note that there is no clear segregation between different Seyfert types or the DPE subsample based on accretion rate. In considering the disk-wind paradigm for disk emitters, M. Elitzur et al. (2014) noted that there were exceptions to their model, such as some high-Eddington ratio DPEs. It appears that within this X-ray-selected BASS sample, the disk-wind model cannot provide a clear explanation for the differences between DPEs and non-DPE broad-line AGN based on accretion rate alone.

We see no significant differences in the optical and mid-IR variability properties between the DPE and non-DPE broadline AGN samples, in agreement with the variability-selected AGN sample from ZTF (C. Ward et al. 2024). This, in combination with the similar DPE rate for variable ZTF AGN, implies that variability amplitude does not assist in the identification of DPEs—a reflection that the two samples do not have large differences in optical luminosity, accretion rate, and BH mass, which have been found to anti-correlate with variability amplitude (K. Chanchaiworawit & V. Sarajedini 2024). The lack of any significant differences in obscuration tracers such as mid-IR color and column density of obscuring material reflects that within the typical range of inclination angles 0 < i < 30 for the two populations, we do not see much to distinguish the $i > 14^{\circ}$ DPEs from the $i < 14^{\circ}$ AGN, where the shoulders of a disk profile would not be distinguishable.

The presence of the disk profile can result in over-estimation of the virial BH mass measured from the broad-line FWHM. Given the dependence of the profile width on disk parameters that are uncorrelated with mass, such as disk viewing angle, and parameters that may only be loosely correlated with BH mass, including the turbulent broadening parameter, it is difficult to obtain correct virial masses for DPEs. In Figure 13,

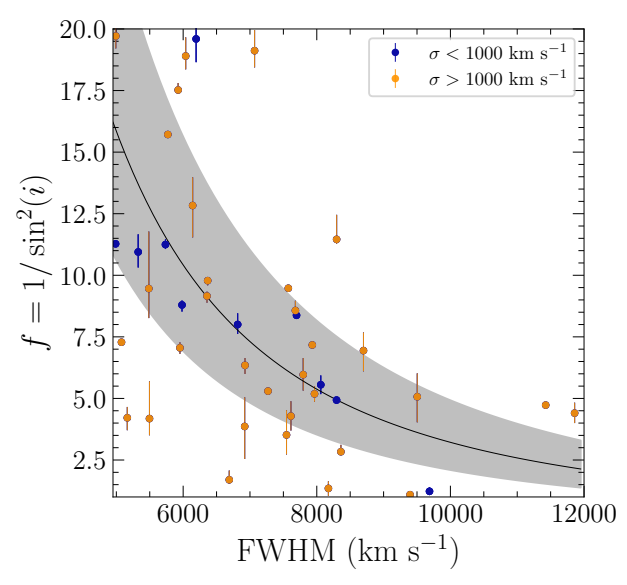


Figure 13. Relationship between the sine of the inclination angle and the FWHM of the broad line for the DPEs, split into populations with a small $\sigma < 1000~\rm km~s^{-1}$ broadening parameter and a large $\sigma > 1000~\rm km~s^{-1}$ broadening parameter. The black curve and gray shaded region denote the relation and dispersion found from simulations of disk profiles across inclination for DPEs with $\sigma = 733~\pm~189$ reported in T. Storchi-Bergmann et al. (2017).

we show the relationship between the sine of the inclination angle and the FWHM of the broad line for the DPEs, split into populations with small $(\sigma < 1000 \,\mathrm{km \, s^{-1}})$ and large $(\sigma > 1000 \,\mathrm{km \, s}^{-1})$ broadening parameters. For comparison, we show the relation found from simulations of disk profiles across inclination with the average properties of the five DPEs in the sample of Type 1 Seyferts from the Palomar Spectroscopic Survey (A. V. Filippenko & W. L. W. Sargent 1985; L. C. Ho et al. 1995), which had $\sigma = 733 \pm 189$, $\eta_1 = 1575 \pm 125$, and $\eta_2 = 3433 \pm 1211$ (T. Storchi-Bergmann et al. 2017). For objects with an FWHM within the range of 5000–12,000 km s⁻¹ covered by the original paper, only those with intermediate inclination angles and a low broadening parameter similar to the Palomar DPEs have a predictable relationship between FWHM and inclination angle. This demonstrates that both the inclination angle and the level of turbulent broadening—and degeneracies between the two must be understood when identifying DPE candidates and correcting for the effect of the disk properties on the width of the broad line.

We note that two DPE candidates have been identified as changing-look AGN (CLAGN) or CLAGN candidates due to changes in their ${\rm H}\alpha$ and ${\rm H}\beta$ broad-line flux over time. BAT 1194 (IRAS 23226–3843) was classified as a CLAGN during a flaring event in 2019, where it showed double-peaked broad lines with a different shape compared to archival 1999 spectra (W. Kollatschny et al. 2020). BAT 862 (LEDA 1659236) was identified as a CLAGN candidate due to a decrease in broadline flux and a change in velocity structure observed in a 2020 spectrum compared to archival data in 2004 (M. J. Temple et al. 2023). The presence of one to two CLAGN in a sample of 71 DPEs is consistent with the 0.7%–6.2% fraction observed for BASS AGN overall (M. J. Temple et al. 2023).

The differences that we observe between the DPE and non-DPE samples, including the high X-ray luminosities, low Eddington ratios, higher [O I]/H α line ratios, and earlier host

type morphologies, point toward a physical difference in the BLR structure of the two populations. These differences may be even stronger if the unidentifiable disk emitters at low inclination angles could be identified and removed from the non-DPE sample. The fact that 15% of DPEs contained both a single- and double-peaked contribution to the broad line indicates that some AGN are also in a transitional state between the two BLR geometries. To disentangle physical differences from viewing angle effects, further work on identifying face-on DPEs and DPEs with both a single and double-peaked component is needed. Given the degeneracies introduced by modeling both a double-peaked disk profile and a central Gaussian BLR, which fills the region between the peaks, it can be very difficult to determine if an AGN contains both components based on a single-epoch spectrum. Multiepoch spectroscopy may be an essential way to confirm disk emission in multicomponent broad lines: in previous spectroscopic monitoring programs of AGN, analysis of the "root mean square" spectra, which often showed a double-peaked H β profile implying the presence of variable, disk-like gas that may not be clear from a spectrum that appears single peaked (K. D. Denney et al. 2010; J. S. Schimoia et al. 2017; T. Storchi-Bergmann et al. 2017). Outflows also play a role in the quality of the disk models and DPE classifications: given that 55% of Sy1.9s and 46% of Sy1s in BASS DR1 had wings in the O[III] narrow lines, indicating the presence of outflows (A. F. Rojas et al. 2020), an outflowing component may improve the modeling of 50% of the DPEs.

Aside from identifying the variable disk components in "rms" spectra, analysis of the double-peaked profiles across UV/optical lines may be beneficial for understanding the different BLR components. Double-peaked near-IR lines also prove to be a useful probe: the recent detection of O I λ 11297, Pa α , and tentative He I λ 10830 double-peaked broad lines with an additional Gaussian broad component in local Sy1 galaxy III Zw 002 demonstrated this (D. Dias dos Santos et al. 2023). Most recently, double-peaked profiles of the NIR Ca II triplet and O I λ 8446 were identified in NGC 4593 (M. W. Ochmann et al. 2025). UV and near-IR spectroscopy of the BASS DPEs would enable more comprehensive disk modeling across multiple double-peaked line profiles.

Another opportunity to map the structure of the BLR region in DPEs is possible using the new capabilities of the Resolve X-ray calorimeter (Y. Ishisaki et al. 2022) on the new X-ray Imaging and Spectroscopy Mission (XRISM; M. Tashiro et al. 2020), which provides a resolution of $\Delta E \approx 4.5 \, \text{eV}$ across the 1.6–17.4 keV passband. XRISM/Resolve spectroscopy of the Fe K α complex of broad-line AGN NGC 4151 showed that the line width was comparable with the broad H β line (Xrism Collaboration et al. 2024). Modeling of the Fe K α line shape enabled separate detection of emission from the BLR at $\xi \sim 3 \times 10^3$, the inner edge of the dusty torus at $\xi \sim 10^4$, and warps at $\xi \sim 100$ (Xrism Collaboration et al. 2024). XRISM/ Resolve observations of X-ray bright DPEs like BAT 1183 (Mrk 926) could search for a double-peaked broad component to the Fe K α line to aid interpretation of the BLR geometry implied by modeling of the Balmer lines.

8. Conclusions

In this paper, we have undertaken a population study of a hard X-ray selected and flux-limited sample of 343 Swift-BAT AGN from the BASS survey with optical spectroscopy,

indicating the presence of broad H α lines, providing a large sample of AGN that is unbiased to inclination angle or other selection effects introduced by optical spectroscopy. We fit the broad H α profiles with double-peaked disk models to systematically classify DPEs and AGN without double-peaked profiles, and report the disk properties of 71 DPEs (Table 2), leading to the following findings.

First, we find that >21% of BASS AGN with broad ${\rm H}\alpha$ emission have double-peaked disk profiles, similar to the rate found for variability-selected AGN (C. Ward et al. 2024) and radio-loud broad-line AGN (M. Eracleous & J. P. Halpern 2003). As disk profiles introduce biases to virial mass measurements, this indicates that the presence of DPEs could introduce biases in the $M_{\rm BH}$ – σ_* relation if they are unidentified in massive BH populations. As the FWHM of the broad-line profile depends significantly on both inclination angle and the level of turbulent broadening in the disk (Figure 13), it is challenging to correct for the level of broadening introduced by the disk profile and caution must be taken when DPEs contaminate large samples used for $M_{\rm BH}$ – σ_* studies.

Second, we confirm with this large, systematically classified sample that DPEs have intrinsically higher masses by ~ 0.4 dex and lower Eddington ratios by ~ 0.3 dex than non-DPE broad-line AGN when using BH masses estimated from stellar dispersion velocities, where the presence of the disk profile will not inhibit accurate mass measurement. DPEs also have a preference for elliptical hosts, higher X-ray luminosities —with a median value that is 0.47 dex greater than non-DPEs —and higher [O I] $\lambda 6306/H\alpha$ flux ratios when compared to the non-DPE broad-line AGN sample. The DPEs also had subarcsecond 22 GHz radio luminosities that were \sim 0.3 dex higher than the non-DPEs, and extended 1 GHz radio luminosities that were more likely to fall in the high $L_{1 \text{ GHz}} = 39-42 \text{ (erg s}^{-1}) \text{ range, but larger samples are}$ required to find stronger evidence that the radio luminosities of the two populations are from different distributions. Despite the differences in masses, accretion rates, and X-ray and radio luminosities, DPEs are not significantly segregated from non-DPE broad-line AGN in the $L_{\rm bol}$ versus $M_{\rm BH}$ relation and do not show a preference for intermediate Seyfert types over Syls, suggesting that accretion rate changes alone in the context of the disk-wind model may not be able to account for the transition to a disk profile. This finding for hard X-rayselected AGN contrasts with previous findings for spectroscopically selected AGN samples (M. Elitzur et al. 2014).

Finally, in this sample, we do not find differences across a wide range of multiwavelength properties when comparing DPEs to non-DPE broad-line AGN, including optical and mid-IR variability levels, WISE colors, Fe K α equivalent width, the Balmer decrement, $\alpha_{\rm ox}$, the column density of neutral obscuring material $N_{\rm H}$, and the rate of changing-look events. The challenge of identifying DPEs at low inclination angles may be inhibiting the clean separation of DPEs and non-DPE broad-line AGN. Further work is required to disentangle physical differences and viewing angle selection effects if we are to understand the different accretion geometries and observational properties of these systems.

Acknowledgments

We would like to thank the anonymous referee for their helpful comments. We acknowledge support from NASA through ADAP award 80NSSC22K1126 (M.K.), ANID

Fondecyt Regular grants 1230345 (CR),1241005, and 1250821 (F.E.B., E.T.), ANID BASAL project FB210003 (C.R., F.E.B., E.T.), Millennium Science Initiative—AIM23-0001 and ICN12 009 (F.E.B.), and the China-Chile joint research fund (CR). B.T. acknowledges support from the European Research Council (ERC) under the European Union's Horizon 2020 research and innovation program (grant agreement number 950533). I.M.C. acknowledges support from ANID program FONDECYT Postdoctorado 3230653. K.O. acknowledges support from the Korea Astronomy and Space Science Institute under the R&D program (Project No. 2025-1-831-01), supervised by the Korea AeroSpace Administration, and the National Research Foundation of Korea (NRF) grant funded by the Korea government (MSIT) (RS-2025-00553982). A.J. acknowledges support from the FONDECYT Postdoctoral fellowship 3230303.

This research has made use of the CIRADA cutout service, ²⁶ operated by the Canadian Initiative for Radio Astronomy Data Analysis (CIRADA). CIRADA is funded by a grant from the Canada Foundation for Innovation 2017 Innovation Fund (Project 35999), as well as by the Provinces of Ontario, British Columbia, Alberta, Manitoba, and Quebec,

in collaboration with the National Research Council of Canada, the US National Radio Astronomy Observatory, and Australia's Commonwealth Scientific and Industrial Research Organization.

This publication also makes use of data products from NEOWISE, which is a project of the Jet Propulsion Laboratory/California Institute of Technology, funded by the Planetary Science Division of the National Aeronautics and Space Administration.

This research has made use of the NASA/IPAC Infrared Science Archive, which is funded by the National Aeronautics and Space Administration and operated by the California Institute of Technology.

Software: astropy (Astropy Collaboration et al. 2013, 2018, 2022), pPXF (M. Cappellari 2017), SciPy (P. Virtanen et al. 2020).

Appendix

We summarize the properties of the non-DPE broad-line AGN sample in Table 4.

 Table 4

 Properties of the 272 Non-DPE Broad-line AGN from the BASS Broad-line AGN Sample

Swift-											
BAT					Galaxy			ZTF	WISE		
ID	R.A.	Decl.	z	Type	Morphology	W2	W1 - W2	variance	χ^2/dof	VLASS 3 GHz	RACS 1 GHz
	(hh:mm:ss)	(dms)				(mag)	(mag)			(mJy)	(mJy)
(1)	(2)	(3)	(4)	(5)	(6)	(7)	(8)	(9)	(10)	(11)	(12)
2	00:01:46.08	-76:57:14.40	0.058	Sy1.5	Merger	10.6	0.84	•••	904.52	•••	6.48 ± 1.14
3	00:02:26.42	+03:21:06.84	0.025	Sy1.2	Disk-spiral	10.27	0.61	0.07	846.56	ND	8.77 ± 1.68
6	00:06:19.54	+20:12:10.80	0.0262	Sy1.2	Pointlike	7.84	0.89	0.06	1540.96	4.97 ± 0.31	
14	00:26:40.68	-53:09:47.88	0.062	Sy1.5	Smooth	10.75	0.67	•••	2109.13	•••	$1.44 ~\pm~ 0.7$
22	00:36:20.95	+45:39:53.64	0.0477	Sy1.2	Disk-spiral	9.89	0.76	0.07	204.51	ND	
29	00:43:01.90	+30:17:19.68	0.052	Sy1.9	Smooth	10.46	0.85	0.61	1246.27	1.4 ± 0.32	
36	00:51:54.77	+17:25:58.44	0.0649	Sy1.2	Smooth	10.8	0.96	0.06	22.58	ND	
39	00:54:52.13	+25:25:39.00	0.155	Sy1.5	Smooth	10.19	1.01	0.1	581.49	1.23 ± 0.29	3.08 ± 0.91
51	01:05:38.81	-14:16:13.44	0.0664	Sy1.5	Other/unc.	10.21	1.12	0.05	777.73	$3.81 ~\pm~ 0.24$	8.73 ± 1.34
55	01:07:39.65	-11:39:11.16	0.0466	Sy1.8	Edge-on	10.58	0.96	0.03	17.91	$5.67 ~\pm~ 0.85$	10.57 ± 1.68
60	01:13:51.05	+13:16:18.48	0.049	Sy1.5	Merger	9.05	0.95	0.03	106.93	5.9 ± 0.28	15.78 ± 2.08
65	01:16:31.15	-12:36:16.92	0.1425	Sy1.8	Smooth	11.35	1.05	•••	134.64	$3.6~\pm~0.25$	5.59 ± 1.24
72	01:23:54.36	-35:03:55.44	0.019	Sy1.9	Merger	7.92	0.95	•••	671.11	$5.96~\pm~0.28$	19.02 ± 1.98
73	01:23:45.77	-58:48:20.88	0.047	Sy1.2	Merger	7.94	0.98	•••	327.31	•••	5.84 ± 1.02
75	01:25:55.94	+35:10:36.84	0.3119	Sy1	Smooth	9.82	1.0	0.12	208.14	18.79 ± 0.23	•••
78	01:28:06.72	-18:48:30.96	0.046	Sy1.5	Disk-spiral	9.92	0.87	0.02	3940.59	1.92 ± 0.39	4.06 ± 1.02
80	01:29:07.66	-60:38:42.00	0.2036	Sy1.8	Merger	12.13	0.94	•••	86.33	•••	13.85 ± 1.59
85	01:34:45.62	-04:30:13.32	0.079	Sy1.5	Smooth	10.9	0.76	0.59	1441.62	1.21 ± 0.3	•••
88	01:39:24.00	+29:24:07.20	0.072	Sy1.5	Merger	11.12	0.42	0.11	84.4	$2.96~\pm~0.32$	•••
89	01:40:26.81	-53:19:39.36	0.0716	Sy1.5	Smooth	10.86	1.0		3373.91		11.28 ± 1.35
92	01:48:59.69	+21:45:33.84	0.0691	Sy1.2	Smooth	12.29	0.2	0.49	62.6	ND	•••
98	01:55:24.96	+02:28:16.68	0.0828	Sy1	Smooth	10.44	0.87	0.52	1073.76	$1.55 ~\pm~ 0.28$	•••
99	01:57:10.94	+47:15:59.04	0.048	Sy1.2	Disk-spiral	10.94	0.59	1.59	565.53	ND	•••

Note. Properties of the 272 BASS AGN that were not classified as DPEs and served as a non-DPE broad-line AGN sample. Column (1): BAT ID number from M. J. Koss et al. (2022a). Columns (2)–(3): R.A. and decl. of the BAT counterpart from M. J. Koss et al. (2022a). Column (4): spectroscopic redshift from M. J. Koss et al. (2022a). Column (5): Seyfert classification from K. Oh et al. (2022). Column (6): galaxy morphology classification from M. Parra Tello et al. (2025). Columns (7) and (8): median W2 magnitude and median W1 — W2 color across the NEOWISE light curves. Column (9): excess variance from the *g*-band ZTF light curves. Column (10): χ^2 /dof of the WISE W2 light curves. Column (11): 2–4 GHz radio flux from VLASS for epoch 1 (2017–2018), with 2.5 beam, where ND indicates radio nondetection and dash indicates that the source was not within the surveyed region. Column (12): 1 GHz radio flux from ASKAP-RACS, with 15" resolution. (This table is available in its entirety in machine-readable form in the online article.)

-

²⁶ http://cutouts.cirada.ca/

ORCID iDs

Charlotte Ward https://orcid.org/0000-0002-4557-6682 Michael J. Koss https://orcid.org/0000-0002-7998-9581 Michael Eracleous https://orcid.org/0000-0002-3719-940X Benny Trakhtenbrot https://orcid.org/0000-0002-3683-7297 Franz E. Bauer https://orcid.org/0000-0002-8686-8737 Turgay Caglar https://orcid.org/0000-0002-9144-2255 Fiona Harrison https://orcid.org/0000-0002-4226-8959 Arghajit Jana https://orcid.org/0000-0001-7500-5752 Darshan Kakkad https://orcid.org/0000-0002-2603-2639 Macon Magno https://orcid.org/0000-0002-1292-1451 Ignacio del Moral-Castro https://orcid.org/0000-0001-8931-1152 Richard Mushotzky https://orcid.org/0000-0002-7962-5446 Kyuseok Oh https://orcid.org/0000-0002-5037-951X Alessandro Peca https://orcid.org/0000-0003-2196-3298 Meredith C. Powell https://orcid.org/0000-0003-2284-8603 Claudio Ricci https://orcid.org/0000-0001-5231-2645 Alejandra Rojas https://orcid.org/0000-0003-0006-8681 Krista Lynne Smith https://orcid.org/0000-0001-5785-7038 Daniel Stern https://orcid.org/0000-0003-2686-9241 Ezequiel Treister • https://orcid.org/0000-0001-7568-6412 C. Megan Urry https://orcid.org/0000-0002-0745-9792

```
References
Assef, R. J., Stern, D., Kochanek, C. S., et al. 2013, ApJ, 772, 26
Astropy Collaboration, Price-Whelan, A. M., Sipőcz, B. M., et al. 2018, AJ,
Astropy Collaboration, Price-Whelan, A. M., Lim, P. L., et al. 2022, ApJ,
   935, 167
Astropy Collaboration, Robitaille, T. P., Tollerud, E. J., et al. 2013, A&A,
   558, A33
Baldwin, J. A., Phillips, M. M., & Terlevich, R. 1981, PASP, 93, 5
Ball, G. H., Narayan, R., & Quataert, E. 2001, ApJ, 552, 221
Bellm, E. C., Kulkarni, S. R., Graham, M. J., et al. 2019, PASP, 131, 018002
Bentz, M. C., Peterson, B. M., Netzer, H., Pogge, R. W., & Vestergaard, M.
   2009, ApJ, 697, 160
Bian, W., Chen, Y., Gu, Q., & Wang, J. 2007, ApJ, 668, 721
Bramich, D. M., Vidrih, S., Wyrzykowski, L., et al. 2008, MNRAS, 386, 887
Caglar, T., Burtscher, L., Brandl, B., et al. 2020, A&A, 634, A114
Caglar, T., Koss, M. J., Burtscher, L., et al. 2023, ApJ, 956, 60
Cappellari, M. 2017, MNRAS, 466, 798
Cappellari, M., & Emsellem, E. 2003, PASP, 116, 138
Chajet, L. S., & Hall, P. B. 2013, MNRAS, 429, 3214
Chanchaiworawit, K., & Sarajedini, V. 2024, ApJ, 969, 131
Chen, K., & Halpern, J. P. 1989, ApJ, 344, 115
Czerny, B., Du, P., Wang, J.-M., & Karas, V. 2016, ApJ, 832, 15
Czerny, B., Modzelewska, J., Petrogalli, F., et al. 2015, AdSpR, 55, 1806
Dekany, R., Smith, R. M., Riddle, R., et al. 2020, PASP, 132, 038001
den Brok, J. S., Koss, M. J., Trakhtenbrot, B., et al. 2022, ApJS, 261, 7
Denney, K. D., Peterson, B. M., Pogge, R. W., et al. 2010, ApJ, 721, 715
Di Matteo, T., Fabian, A. C., Rees, M. J., Carilli, C. L., & Ivison, R. J. 1999,
     INRAS, 305, 492
Di Matteo, T., Quataert, E., Allen, S. W., Narayan, R., & Fabian, A. C. 2000,
          S, 311, 507
Dias dos Santos, D., Rodríguez-Ardila, A., Panda, S., & Marinello, M. 2023,
   ApJL, 953, L3
Doan, A., Eracleous, M., Runnoe, J. C., et al. 2020, MNRAS, 491, 1104
Drake, A. J., Djorgovski, S. G., Mahabal, A., et al. 2009, ApJ, 696, 870
Elitzur, M., & Ho, L. C. 2009, ApJ, 701, L91
Elitzur, M., Ho, L. C., & Trump, J. R. 2014, MNRAS, 438, 3340
Elitzur, M., & Shlosman, I. 2006, ApJL, 648, L101
Emmering, R. T., Blandford, R. D., & Shlosman, I. 1992, ApJ, 385, 460
Eracleous, M., & Halpern, J. P. 1994, ApJS, 90, 1
Eracleous, M., & Halpern, J. P. 2003, ApJ, 599, 886
Eracleous, M., Halpern, J. P., M. Gilbert, A., Newman, J. A., &
   Filippenko, A. V. 1997, ApJ, 490, 216
Eracleous, M., Lewis, K. T., & Flohic, H. M. 2009, NewAR, 53, 133
Filippenko, A. V., & Sargent, W. L. W. 1985, ApJS, 57, 503
```

```
Foreman-Mackey, D., Hogg, D. W., Lang, D., & Goodman, J. 2013, PASP,
   125, 306
Fu, Y., Cappellari, M., Mao, S., et al. 2023, MNRAS, 524, 5827
Gordon, Y. A., Boyce, M. M., O'Dea, C. P., et al. 2021, ApJS, 255, 30
Goulding, A. D., Greene, J. E., Setton, D. J., et al. 2023, ApJL, 955, L24
Graham, M. J., Kulkarni, S. R., Bellm, E. C., et al. 2019, PASP, 131, 1
Greene, J. E., & Ho, L. C. 2005, ApJ, 630, 122
Greene, J. E., Strader, J., & Ho, L. C. 2020, ARA&A, 58, 257
Guedel, M., & Benz, A. O. 1993, ApJL, 405, L63
Gupta, K. K., Ricci, C., Temple, M. J., et al. 2024, A&A, 691, A203
Hale, C. L., McConnell, D., Thomson, A. J. M., et al. 2021, PASA, 38, e058
Ho, L. C. 2008, ARA&A, 46, 475
Ho, L. C. 2009, ApJ, 699, 626
Ho, L. C., Filippenko, A. V., & Sargent, W. L. 1995, ApJS, 98, 477
Ho, L. C., Filippenko, A. V., Sargent, W. L. W., & Peng, C. Y. 1997, ApJS,
Ho, L. C., Rudnick, G., Rix, H., et al. 2000, ApJ, 541, 120
Ishisaki, Y., Kelley, R. L., Awaki, H., et al. 2022, Proc. SPIE, 12181, 121811S
Jiang, P., Wang, J. X., & Wang, T. G. 2006, ApJ, 644, 725
Kaspi, S., Smith, P. S., Netzer, H., et al. 2000, ApJ, 533, 631
Kauffmann, G., Heckman, T. M., Tremonti, C., et al. 2003, MNRAS, 346, 1055
Kewley, L. J., Dopita, M. A., Sutherland, R. S., Heisler, C. A., & Trevena, J.
Kewley, L. J., Groves, B., Kauffmann, G., & Heckman, T. 2006, MNRAS,
   372, 961
Kollatschny, W. 2003, A&A, 412, L61
Kollatschny, W., Grupe, D., Parker, M. L., et al. 2020, A&A, 638, A91
Komatsu, E., Smith, K. M., Dunkley, J., et al. 2011, ApJS, 192, 18
Kormendy, J., & Ho, L. C. 2013, ARA&A, 51, 511
Koss, M., Trakhtenbrot, B., Ricci, C., et al. 2017, ApJ, 850, 74
Koss, M. J., Ricci, C., Trakhtenbrot, B., et al. 2022a, ApJS, 261, 2
Koss, M. J., Trakhtenbrot, B., Ricci, C., et al. 2022b, ApJS, 261, 1
Lacy, M., Baum, S. A., Chandler, C. J., et al. 2020, PASP, 132, 035001
Laor, A., & Behar, E. 2008, MNRAS, 390, 847
Lewis, K. T., & Eracleous, M. 2006, ApJ, 642, 711
Magno, M., Smith, K. L., Wong, O. I., et al. 2025, ApJ, 981, 202
Mainzer, A., Grav, T., Bauer, J., et al. 2011, ApJ, 743, 156
Mainzer, A., Bauer, J., Cutri, R. M., et al. 2014, ApJ, 792, 30
Masci, F. J., Laher, R. R., Rusholme, B., et al. 2019, PASP, 131, 1
Mejía-Restrepo, J. E., Trakhtenbrot, B., Koss, M. J., et al. 2022, ApJS, 261, 5
Mezcua, M., Pacucci, F., Suh, H., Siudek, M., & Natarajan, P. 2024, ApJL,
   966, L30
Murray, N., & Chiang, J. 1996, Natur, 382, 789
Murray, N., Chiang, J., Grossman, S. A., & Voit, G. M. 1995, ApJ, 451, 498
Nagao, T., Murayama, T., Shioya, Y., & Taniguchi, Y. 2002, ApJ, 567, 73
Nagoshi, S., Iwamuro, F., Yamada, S., et al. 2024, MNRAS, 529, 393
NEOWISE Team 2020, NASA IPAC DataSet, IRSA144,
Netzer, H., & Laor, A. 1993, ApJL, 404, L51
Nguyen, K., Bogdanović, T., Runnoe, J. C., et al. 2018, ApJ, 870, 16
Ochmann, M. W., Weilbacher, P. M., Probst, M. A., et al. 2025, A&A, 697, L5
Oh, K., Koss, M. J., Ueda, Y., et al. 2022, ApJS, 261, 4
Onoue, M., Ding, X., Silverman, J. D., et al. 2024, NatA
Osterbrock, D. E., & Ferland, G. J. 2006, Astrophysics of Gaseous Nebulae
  and Active Galactic Nuclei (2nd ed.; Sausalito, CA: Univ. Science Books)
Page, K. L., O'Brien, P. T., Reeves, J. N., & Turner, M. J. L. 2004, MNR
  347, 316
Park, D., Woo, J.-H., Treu, T., et al. 2012, ApJ, 747, 30
Parra Tello, M., Bauer, F. E., De Cicco, D., et al. 2025, A&A, 700, A111
Peterson, B. M. 1993, PASP, 105, 247
Peterson, B. M. 2014, SSRv, 183, 253
Peterson, B. M., & Wandel, A. 2000, ApJL, 540, L13
Popović, L. Č., Mediavilla, E., Bon, E., & Ilić, D. 2004, A&A, 423, 909
Ricci, C., & Trakhtenbrot, B. 2023, NatAs, 7, 1282
Ricci, C., Trakhtenbrot, B., Koss, M. J., et al. 2017, ApJS, 233, 17
Rojas, A. F., Sani, E., Gavignaud, I., et al. 2020, MNRAS, 491, 5867
Runnoe, J. C., Eracleous, M., Bogdanović, T., Halpern, J. P., & Sigurdsson, S.
   2025, ApJ, 984, 17
Schawinski, K., Thomas, D., Sarzi, M., et al. 2007, MNRAS, 382, 1415
Schimoia, J. S., Storchi-Bergmann, T., Nemmen, R. S., Winge, C., &
   Eracleous, M. 2012, ApJ, 748, 145
Schimoia, J. S., Storchi-Bergmann, T., Winge, C., Nemmen, R. S., &
   Eracleous, M. 2017, MNRAS, 472, 2170
Shen, Y. 2013, BASI, 41, 61
Shen, Y., Greene, J. E., Strauss, M. A., Richards, G. T., & Schneider, D. P.
   2008, ApJ, 680, 169
Shen, Y., Wu, J., Jiang, L., et al. 2019, ApJ, 873, 35
```

Flohic, H. M. L. G., Eracleous, M., & Bogdanović, T. 2012, ApJ, 753, 133

```
Storchi-Bergmann, T., Schimoia, J. S., Peterson, B. M., et al. 2017, ApJ, 835, 236
```

Storchi-Bergmann, T., Nemmen da Silva, R., Eracleous, M., et al. 2003, ApJ, 598, 956

Strateva, I. V., Strauss, M. A., Hao, L., et al. 2003, AJ, 126, 1720
Tashiro, M., Maejima, H., Toda, K., et al. 2020, Proc. SPIE, 11444, 1144422
Temple, M. J., Ricci, C., Koss, M. J., et al. 2023, MNRAS, 518, 2938
Terashima, Y., & Wilson, A. S. 2003, ApJ, 583, 145
Übler, H., Maiolino, R., Curtis-Lake, E., et al. 2023, A&A, 677, A145
Vagnetti, F., Turriziani, S., & Trevese, D. 2011, A&A, 536, A84

```
van Velzen, S., Gezari, S., Hammerstein, E., et al. 2021, ApJ, 908, 4 Virtanen, P., Gommers, R., Oliphant, T. E., et al. 2020, NatMe, 17, 261 Ward, C., Gezari, S., Frederick, S., et al. 2021, ApJ, 913, 102 Ward, C., Gezari, S., Nugent, P., et al. 2022, ApJ, 936, 104 Ward, C., Gezari, S., Nugent, P., et al. 2024, ApJ, 961, 172 Woo, J.-H., Yoon, Y., Park, S., Park, D., & Kim, S. C. 2015, ApJ, 801, 38 Wright, E. L., Eisenhardt, P. R., Mainzer, A. K., et al. 2010, ApJ, 140, 1868 Wu, X., & Liu, F. K. 2004, ApJ, 614, 91 Xrism Collaboration, Audard, M., Awaki, H., et al. 2024, ApJL, 973, L25 Zhang, X.-G., & Feng, L.-L. 2017, MNRAS, 464, 2203
```